This is the peer-reviewed, final accepted version for American Mineralogist, published by the Mineralogical Society of America.
The published version is subject to change. Cite as Authors (Year) Title. American Mineralogist, in press.
DOI: https://doi.org/10.2138/am-2021-7691. http://www.minsocam.org/
Resubmission: American Mineralogist

REVISION 1

A model for the kinetics of high temperature reactions between polydisperse volcanic ash and SO_2 gas

Fabian B. Wadsworth[1,*], Jérémie Vasseur[2], Ana Silvia Casas[2], Pierre Delmelle[3], Kai-Uwe Hess[2], Paul M. Ayris[2], Donald B. Dingwell[2]

[1]Earth Sciences, Durham University, Science Labs, Durham, DH1 3LE, United Kingdom, [2]Earth and Environmental Sciences, Ludwig-Maximilians-Universität, Theresienstr. 41, 80333 Munich, Germany. [3]Earth and Life Institute, Environmental Sciences, Université catholique de Louvain, L7.05.10, 1348 Louvain-la-Neuve, Belgium.

*Corresponding author: fabian.b.wadsworth@durham.ac.uk

Abstract

Rapid calcium diffusion occurs in rhyolitic volcanic ash particles exposed to hot SO_2 atmospheres. Such chemical transport is important immediately following fragmentation, during proximal transport in eruption plumes, and during percolative gas transport through a permeable volcanic edifice. Here we analyze published results of experiments designed to constrain the kinetics of this process. The experiments involve crushed rhyolitic glass particles tumbled in SO_2-bearing atmospheres at a wide range of relevant temperatures. We find that the particle-gas reaction is fed by calcium diffusion from the bulk to the particle surfaces where calcium-sulfate crystals grow. The calcium flux is accommodated by local iron oxidation state changes. This process results in time-dependent concentrations of surface calcium that are leachable in aqueous solutions. Those leachate concentrations represent a proxy for the diffusive flux of Ca^{2+} out of the particle to form the surface deposits. We formulate a mathematical framework to convolve the starting particle size distributions with the solution to Fickian 1-dimensional diffusion, to find a weighted polydisperse result. Using this framework, we minimize for a temperature-dependent calcium diffusivity and compare our results with published calcium diffusivity data. We demonstrate that calcium diffusivity in rhyolite can be decomposed into two regimes: (1) a high temperature regime in which the diffusivity is given by the Eyring equation, and (2) a low-temperature regime more relevant to rhyolite volcanism and these gas-ash reactions. As a further test of our model, we compare the output against spatially-resolved data for the calcium gradients in the experimental particles. Our analysis suggests that surface reaction rates are rapid compared with the diffusion of calcium from the particle to the surface such that full diffusion models must be solved to predict the rhyolite-SO_2 reaction. We conclude by suggesting how this framework could be used to make quantitative predictions of sulfur budgets and iron oxidation during rhyolitic eruptions.

Keywords: scavenging; scrubbing; gas-ash reactions; volcanic eruption

1. Introduction

The release of SO_2 during large volcanic eruptions can affect Earth's climate over timescales of months to years (Bluth et al. 1997; Robock 2000) or perhaps even millennia (Baldini et al. 2015). For recent or ongoing eruptions that occurred during the satellite age, the SO_2 input into the atmosphere can be monitored and quantified directly (e.g. Carn et al. 2017). However, for eruptions that have occurred deeper in Earth's history, the SO_2 budget is more difficult to estimate. The so-called 'sulfur excess' problem is one example of how the sulfur budget of the trans-crustal magma system prior to eruption cannot be derived simply from observed erupted SO_2, and that other processes must play a significant role (Shinohara 2008; Edmonds et al. 2010; Wallace and Edmonds 2011). Here we draw on the experimental observation that hot ash particles at magmatic temperatures can scrub SO_2 from the initial eruptive gas phase (Ayris et al. 2013; Delmelle et al. 2018) – a process for which there remains no general model. Thus, SO_2 scrubbing represents a reaction pathway in the volcanic sulfur cycle that warrants further investigation and which potentially further impacts the relationship between pre-eruptive sulfur and the atmospheric sulfur loading from eruptions.

As magmas fragment, they become a rapidly moving and evolving mixture of ash and volatile gases (a 'dusty gas') and react chemically over relatively short timescales (Ayris et al. 2013, 2014; Delmelle et al. 2018; Renggli and King 2018). Initial experimental results, and their scaling to volcanic conditions, have indicated that reactions between volcanic ash and SO_2 may be sufficiently rapid to result in significant modification of erupted SO_2 budgets during in-conduit and proximal ash transport (Ayris et al. 2013; Delmelle et al. 2018) or during percolation through volcanic domes (Casas et al. 2019). Before these insights can be used to compute the effect of gas-ash reactions on total sulfur budgets in volcanic eruptions quantitatively and reliably, experimental data has to be tested against detailed constitutive models for the kinetics of this reaction.

In natural systems, high temperature SO_2-ash reactions involve the formation and growth of calcium-bearing salt crystals on the surfaces of ash particles (Ayris et al. 2013; Renggli and King 2017, 2018; Renggli et al. 2019). At the range of conditions that have been explored, the dominant salt formed on natural glass is calcium sulfate (Renggli and King 2018), whose generation is rate-limited by the diffusion of calcium to the particle surfaces (Ayris et al. 2013; Delmelle et al. 2018). In turn, that diffusive flux of calcium is affected by both the temperature and the particle size(s) – where high temperatures and small particles render gas-ash reactions more efficient compared with low temperatures or larger particles. These conditions of small particles and high temperatures could be favored in particularly large explosive eruptions on Earth. During eruptions, small particles are produced when fragmentation is vigorous (Kueppers et al. 2006) and high temperatures can be maintained when fragmentation occurs deep, when conduits are wide, or when mass eruption rates are high, such that there is a long insulated transport pathway before cooling in the plume (Ayris et al. 2013). In Fig. 1 we sketch the portion of the volcanic system in which these high-temperature gas-ash reactions may be operative.

Cognate processes involving the interaction between SO_2 gas and silicate glass or rocks have been explored for synthetic glasses (Douglas and Isard 1949; Johnson and Burnett 1993; Burnett et al. 1997; Renggli and King 2018; Renggli et al. 2019), for calcite-SO_2 reactions (Mavrogenes and Blundy 2017a, 2017b; Saadatfar et al. 2020), and as a mechanism for porphyry copper deposit formation (Henley et al. 2015). In all cases, it is proposed that these reaction pathways represent a key component of the volcanic- or crustal- sulfur cycle on Earth and other planets, and yet there is no clear way to make quantitative predictions of the net contribution of these reaction pathways to the volcanic sulfur budgets across all relevant conditions and input parameters. Here, we aim to present a general formulation for the kinetics of these gas-ash reactions for the case where iron is present in the glass. We validate a mathematical model using a large published dataset, which is specific to SO_2 reactions with rhyolite particles (Casas et al. 2019), yet is general in principle and therefore may be easily adapted to other cases of ash and gas composition.

2. Developing a framework for high-temperature gas-ash reactions

Here we present a mathematical framework in which the rates of gas-ash reaction can be predicted. Throughout, while we focus on the case of iron-bearing rhyolite particles interacting with SO_2 gas, we note that the framework we present is general and where relevant we highlight how it could be adapted for other compositions of ash or gas for which the same reaction mechanisms are appropriate.

a. Phenomenology: Iron-bearing ash/glass and SO_2 gas

Sulfate compounds are found on the surface of freshly erupted natural volcanic ash particles, which is inferred to indicate that SO_2-ash reactions have taken place (Rose 1977; Varekamp et al. 1984; Gerlach and McGee 1994; De Hoog et al. 2001; de Moor et al. 2005). Initially, it was proposed that these compounds precipitate from sulfur-bearing liquid droplets or liquid layers on the surface of ash such as H_2SO_4 liquid (Rose 1977), which would then represent a low-temperature leaching and precipitation process. However, Ayris et al. (2013) questioned the importance of the low-temperature process(es) given that most plumes reach altitudes where liquid droplets are less likely to form and where ice-based SO_2 scavenging is less efficient (Textor et al. 2003). As an alternative, a high temperature mechanism of SO_2 scavenging can also explain the presence of sulfate salt crystals on ash surfaces and is instead driven by the diffusion of cations to the surface, feeding the reaction and salt deposition (Douglas and Isard 1949; Ayris et al. 2013, 2014; Delmelle et al. 2018; Casas et al. 2019). Therefore, while low-temperature adsorption or acid droplet leaching and precipitation may be important down-plume and during or after deposition, the in-plume relevant process of interest here is a high temperature one and thus occurs in the presence of significant cation diffusion in the ash particles.

By examining the phenomenological results from previous work on high-temperature reactions between glass and SO_2 (Ayris et al. 2013; Renggli and King 2018; Casas et al. 2019; Renggli et al. 2019), a few key starting points can be identified. In most cases where an experimental glass used was iron-bearing, exposure of glass surfaces to high temperatures results in a time-dependent formation of surface phases of a wide range of compositions: $CaSO_4$, K_2SO_4, $FeSO_4$, Na_2SO_4, $MgSO_4$, $Na_2Ca(SO_4)_2$, and $Al_2(SO_4)_3$, as well as minor other phases (for a review see Renggli and King 2018). Most of this complexity is found in experimental reactions between mafic glasses and SO_2, such as tholeiitic basalts (Johnson and Burnett 1993; Burnett et al. 1997; Palm et al. 2018; Renggli et al. 2019), not only in terms of the diversity of surface phases that crystallize but also a strong dependence on oxygen fugacity. We posit that more silica-rich rhyolitic particles reacting with SO_2 is a comparatively simple system. For the purposes of this work, we focus on experiments between an iron-bearing rhyolitic glass and SO_2 (Ayris et al. 2013; Casas et al. 2019) for which the dominant surface phase is $CaSO_4$.

Ayris et al. (2013) showed that the time-dependent precipitation of $CaSO_4$ on phonolite particle surfaces was coupled with a spatial gradient of calcium in the underlying glass substrate, depleted toward the interface and inferred that similar profiles develop in the interior of particles of other compositions. This implies that diffusion is the dominant mechanism supplying calcium to the reaction sites at the interface, confirming conclusions made by Douglas and Isard (1949) that cation diffusion in the glass is the rate-limiting mechanism controlling the time-evolution of this family of gas-glass reactions. Ayris et al. (2013) applied simplified diffusion models to their experimental data, treating the time-dependent mass of calcium in the surficial calcium sulfate deposits as a proxy for the diffusive flux of calcium out of the particles. The rate of increase of mass of the salts deposited scales non-linearly with temperature, and particle size (Ayris et al. 2013; Casas et al. 2019). Taken together, these observations suggest that a full diffusion model for calcium fluxes driven by the chemical potential exerted by the presence of SO_2 can be a reasonable way to build a predictive model for the rates of gas-ash reactions.

While experimental evidence appears to confirm that calcium diffusion rates are the limiting processes controlling the kinetics in rhyolite-SO_2 reactions, it clearly also takes a finite time for the nucleation and growth of the crystalline surface phases (Douglas and Isard 1949; Ayris et al. 2013; Delmelle et al. 2018; Renggli and King 2018; Renggli et al. 2019). Therefore, there are two processes at play: (1) calcium moves from the particle bulk to the surface, and (2) the surface reaction(s) must occur. Presumably overall, the process of gas-ash reactions will occur at the rate of whichever of these two processes is the slowest; which remains untested. Ayris et al. (2013) proposed that the surface reaction first forms $CaSO_3$, which then oxidizes to form $CaSO_4$, requiring additional molecular oxygen. However, no direct evidence for surface $CaSO_3$ has been found by experiment. Instead, $CaSO_4$ could form directly, consistent with observations and without the need for additional second-step oxidation of the surface (Henley et al. 2015; Palm et al. 2018; King et al. 2018). Either way, the relative importance of these surface reactions to the overall rate of the process is poorly understood in rhyolites.

b. Diffusion in monodisperse particles

Diffusion acts on timescales $\lambda_{\mathcal{D}} \propto L^2/\mathcal{D}$ or, equivalently over lengthscales $L \propto \sqrt{\mathcal{D}t}$, where $\lambda_{\mathcal{D}}$ is the characteristic diffusion time, L is a characteristic diffusion length, t is the time since the onset of diffusion, and $\mathcal{D}$ is the diffusivity that is variably dependent on temperature, pressure, and the total local concentration of the diffusing species (Crank 1975; Zhang and Cherniak 2010). These relationships provide a useful approximation for scaling diffusion problems and are especially accurate when $\mathcal{D}$ can be taken to be constant. Such cases of constant $\mathcal{D}$ only strictly exist when the system of concern is both isothermal and isobaric, and when the absolute variation in concentration across the concentration profile is small. However, in most applied cases of interest, magmas are non-isothermal, polybaric, and the concentration gradients are large compared with the absolute concentration at equilibrium, making $\mathcal{D}$ a function of both time and spatial position, and potentially invalidating the simplest scaling tools. In such cases, a full diffusion solution is needed along with a relationship between $\mathcal{D}$ and the system temperature, pressure, and local concentration. To meet this need, there has been a large body of work invested in the determination and systemization of diffusivities of many cations of magmatic relevance in a wide variety of liquid or glass compositions and conditions (Jambon 1982; Dingwell 1990; Mungall et al. 1999; Zhang et al. 2010).

For the purposes of understanding diffusion in volcanic particles, Fick's law for diffusive mass transport applies which is $\partial C/\partial t = \nabla(\mathcal{D}\nabla C)$ where C is the concentration of the species of interest (throughout this work unless otherwise stated, C refers to the wt.% value of calcium). For practical purposes, a spherical approximation for geometry is often used for volcanic particles (Wadsworth et al. 2017b). When cast in spherical coordinates Fick's general law becomes (Crank 1975)

$$\frac{\partial C}{\partial t} = \frac{1}{r^2}\frac{\partial}{\partial r}\left(r^2 \mathcal{D}\frac{\partial C}{\partial r}\right), \qquad \text{Eq. 1}$$

where r is the radial spatial position in the sphere measured from the centre. In order to compare solutions to Eq. 1 across a wide range of conditions, it is useful to render Eq. 1 dimensionless by making the following substitutions where a bar above a parameter denotes its dimensionless form

$$\bar{r} = \frac{r}{R};\ \bar{C} = \frac{C}{C_r};\ \bar{t}_r = \frac{t}{\lambda};\ \bar{\mathcal{D}} = \frac{\mathcal{D}}{\mathcal{D}_r};\ \mathrm{Fi}_r = \frac{\mathcal{D}_r}{R^2}\lambda \qquad \text{Eq. 2}$$

where R is the radius of the particle sphere, C_r is a reference concentration, λ is a reference time such that $\bar{t}_r$ is the normalization of time relative to that reference and $\mathcal{D}_r$ is a reference diffusivity. Fi_r is a reference Fick number which is the value of the Fick number at a time of λ and using the reference coefficient of diffusion. The general Fick number is then a dimensionless diffusion time and is given by $\mathrm{Fi} = t/\lambda_{\mathcal{D}} = \mathcal{D}t/R^2$ where $\lambda_{\mathcal{D}}$ is the diffusion timescale. We pick λ to be an arbitrarily long time – longer than the time window of interest, which does not affect the result. Now Eq. 1 can be written in dimensionless form:

$$\frac{\partial \bar{C}}{\partial \bar{t}_r} = \frac{\mathrm{Fi}_r}{\bar{r}^2}\frac{\partial}{\partial \bar{r}}\left(\bar{r}^2 \bar{\mathcal{D}}\frac{\partial \bar{C}}{\partial \bar{r}}\right). \quad \text{Eq. 3}$$

The diffusivity $\mathcal{D}$ is typically dependent on temperature T via an Arrhenian relationship that is linear when $\ln(\mathcal{D})$ is compared with $1/T$. Equivalently

$$\mathcal{D}(T) = \mathcal{D}_\alpha \exp\left(-\frac{\alpha}{T}\right) \quad \text{Eq. 4}$$

and where $\mathcal{D}_\alpha$ and α are empirical coefficients that are usually determined by experiment. For some chemical components that diffuse through volcanic materials, $\mathcal{D}$ is also a function of the absolute concentration C at all local spatial positions. This is the case, for example, for the diffusivity of molecular or total water in rhyolites (Zhang and Ni 2010). When this has been shown to be the case, a different form of $\mathcal{D}(T)$ is often used, which is still Arrhenian but which depends on the total concentration of the diffusing species. The dependence on C is either linear (e.g. for the case of water diffusion in rhyolites; Zhang and Ni 2010), or exponential (e.g. in the case of magnesium diffusion in olivine; Morioka 1981). Here, we acknowledge that this may be the case for calcium diffusion in rhyolite and so explore functional forms for $\mathcal{D}(T, C)$. These variations on Eq. 4 for the case of a dependence of $\mathcal{D}$ on C are

$$\mathcal{D}(T, C) = \mathcal{D}_\beta \exp\left(-\frac{\beta}{T}\right) C, \quad \text{Eq. 5a}$$

$$\mathcal{D}(T, C) = \mathcal{D}_\gamma \exp\left(-\frac{\gamma}{T}\right) \exp(C) \quad \text{Eq. 5b}$$

where, like $\mathcal{D}_\alpha$ and α in Eq. 4, $\mathcal{D}_\beta$, $\mathcal{D}_\gamma$, β, and γ are coefficients that are usually determined by experiment. Eqs 4-5 can then be rendered dimensionless by taking the following substitutions

$$\bar{T} = \frac{T}{T_r};\ \bar{\alpha} = \frac{\alpha}{T_r};\ \bar{\beta} = \frac{\beta}{T_r};\ \bar{\gamma} = \frac{\gamma}{T_r} \quad \text{Eq. 6}$$

where T_r is a reference temperature. Now $\mathcal{D}_r$ in Eq. 2 can be defined as the diffusivity at a temperature of T_r as $\mathcal{D}_r = \mathcal{D}_\alpha \exp(-\alpha/T_r)$, $\mathcal{D}_r = \mathcal{D}_\beta \exp(-\beta/T_r)C_r$, or $\mathcal{D}_r = \mathcal{D}_\gamma \exp(-\gamma/T_r)\exp(C_r)$ in the case of Eq. 4 or Eq. 5, respectively. Eqs 4-5 can be cast in dimensionless form as:

$$\bar{\mathcal{D}} = \exp\left[\bar{\alpha}\left(1 - \frac{1}{\bar{T}}\right)\right], \quad \text{Eq. 7a}$$

$$\bar{\mathcal{D}} = \exp\left[\bar{\beta}\left(1 - \frac{1}{\bar{T}}\right)\right]\bar{C}, \quad \text{Eq. 7b}$$

$$\bar{\mathcal{D}} = \exp\left[\bar{\gamma}\left(1 - \frac{1}{\bar{T}}\right)\right]\exp(\bar{C}). \quad \text{Eq. 7c}$$

If the temperature is constant, then Eq. 7a reduces to $\bar{\mathcal{D}} = 1$, Eq. 7b reduces to $\bar{\mathcal{D}} = \bar{C}$ and Eq. 7c reduces to $\bar{\mathcal{D}} = \exp(\bar{C})$.

For any diffusion problem in a particle sphere, we can now solve Eq. 3 using either Eq. 7a (temperature dependent diffusion), Eq. 7b (temperature and linear concentration dependent diffusion), or Eq. 7c (temperature and exponential concentration dependent diffusion) for different scenarios. We do this by using a finite difference implicit numerical scheme (a so-called 'backwards time, centered space' scheme) with a relaxed fixed-point method to ensure convergence at each time step. The dimensionless temporal and spatial resolutions we use are 10^{-3} and 10^{-2}, respectively. To convert the solution for $d\bar{C}/d\bar{t}_r$ back to a dimensional answer, C_r and T_r would have to be defined, which is specific to the problem in question and is therefore discussed later. Specific numerical approaches for incorporating the concentration dependence of diffusivity are given for the problem of hydrating legumes during soaking in Hsu (1983).

c. Initial conditions, boundary conditions, and reaction rates

To solve Eq. 3 (or Eq. 1), we must define boundary and initial conditions. Our initial condition is taken such that $C = C_i$ for all r, where C_i is the initial concentration in the glass before diffusion begins, and that the concentration outside the particle in the gas phase is zero. At the particle centre $r = 0$, we take Neumann boundary $\mathcal{D}dC/dr = 0$ for all t. At the particle rim $r = R$, for $t > 0$ we have two possible choices

$$C = C_x \quad \text{Eq. 8a}$$

$$\mathcal{D}\frac{dC}{dr} = H(C_\infty - C) \quad \text{Eq. 8b}$$

where Eq. 8a represents a constant boundary value and assumes that the concentration immediately falls to C_x at $r = R$ for all $t > 0$. Eq. 8b represents a boundary reaction term, where H is a reaction rate constant (in $\mathrm{m.s^{-1}}$). From a physico-chemical perspective, it is reasonable to assume that there is a timescale associated with the reaction between calcium being diffused to the surface of the particles

and the SO_2 gas. Previous work has not proved the extent to which this reaction rate is strictly important in these problems of gas-ash reactions, or if it can be neglected. In order to determine its importance, this reaction timescale can be scaled for by $\lambda_{\mathrm{Bi}} \approx R/H$ where λ_{Bi} is a Biot timescale. A Biot number $\mathrm{Bi} = \lambda_{\mathcal{D}}/\lambda_{\mathrm{Bi}} = HR/\mathcal{D}$ is a measure of the relative importance of boundary mass transfer (limited by H) and the internal mass transfer (limited by $\mathcal{D}$). We anticipate that $\mathrm{Bi} \gg 1$ is the regime where the reaction rate at the surface is sufficiently rapid to not impede the process and therefore can be neglected, whereas $\mathrm{Bi} \ll 1$ is the regime where the reaction rate is sluggish and must be accounted for via Eq. 8b.

As before, we render the boundary and initial conditions dimensionless so that initially $\bar{C} = 1$ for all $\bar{r}$, and the boundaries are: (1) at $\bar{r} = 0$, we have $\overline{\mathcal{D}} d\bar{C}/d\bar{r} = 0$ for all $\bar{t}$, and (2) at $\bar{r} = 1$, Eq. 8a is $\bar{C} = 0$ or Eq. 8b is $\overline{\mathcal{D}} d\bar{C}/d\bar{r} = \mathrm{Bi}_{\mathrm{r}}(\bar{C}_{\infty} - \bar{C})$, where Bi_{r} is the reference Biot number at the reference temperature T_r.

d. Gradients of diffusivity and bulk fluxes

A model solution to Eq. 3 is explicitly solvable as described above. If experimental data is spatially resolved – for example in the case of electron microprobe analysis transects along a quenched diffusion profile– then no conversion for bulk fluxes would be required and the data can be directly compared with model solutions. However, it is useful to understand bulk flux data and not just spatially-resolved data – for example, in the case of time-dependent extraction of an element from the surface of a bulk sample particle (Ayris et al. 2013; Casas et al. 2019), as used here. In this case, the bulk data need converting before they can be directly compared to a diffusion model.

To non-dimensionalize time, we give the diffusion timescale in Eq. 2 as $\lambda_{\mathcal{D}} = R^2/\mathcal{D}$ which is strictly valid when used to normalize time in spatially resolved diffusion solutions. However, to scale experimental data in which the diffusivity varies spatially, such as in the case of a concentration-dependent diffusivity, or in non-isothermal conditions, we have to redefine $\lambda_{\mathcal{D}}$.

If we take the case where diffusivity is dependent on temperature but not on concentration, and if we take a scenario where any given test-case is isothermal, then $\overline{\mathcal{D}} = 1$ and $\lambda_{\mathcal{D}}$ is as given in Eq. 2. However, in the case where the diffusivity is dependent on concentration (i.e. Eqs 7b & 7c), then diffusion will induce a spatial gradient of C and therefore of $\mathcal{D}$, requiring that we recast $\lambda_{\mathcal{D}}$. To do this we simply convert the spatial gradient of C into a spatial gradient of $\mathcal{D}$ via Eq. 5 and then average $\mathcal{D}$ over the spatial positions in the sphere giving $\langle\mathcal{D}\rangle$ by:

$$\langle\mathcal{D}\rangle = \frac{\int_0^1 \bar{r}^2 \mathcal{D}\, d\bar{r}}{\int_0^1 \bar{r}^2\, d\bar{r}} \qquad \text{Eq. 9}$$

so that for any isothermal monodisperse sphere diffusion problem, $\lambda_{\mathcal{D}} = R^2/\langle\mathcal{D}\rangle$. For isothermal problems, because $\overline{\mathcal{D}} = \bar{C}$, then $\langle\mathcal{D}\rangle/\mathcal{D}_r$ – termed $\langle\overline{\mathcal{D}}\rangle$ – is the same as $\langle C\rangle/C_r$ – termed $\langle\bar{C}\rangle$ – implying that it does not matter whether the concentration or diffusivity is integrated.

For non-isothermal conditions, we could additionally integrate the change in $\langle\mathcal{D}\rangle$ with the evolution in T to get a dimensionless time $\bar{t} = 1/R^2 \int_{t_i}^{t} \langle\mathcal{D}\rangle\, dt$ where t_i is the initial time of diffusion. However, in the present work we only deal with isothermal datasets so that, while the temperature varies from experiment to experiment, it does not vary with time in a single experiment.

e. Polydisperse distributions of particles

In general, the polydispersivity of a distribution of spheres is captured by $S = \langle R^2 \rangle \langle R \rangle / \langle R^3 \rangle$ where $\langle R^n \rangle$ is the nth moment of the distribution (Torquato 2013; Wadsworth et al. 2017a; Vasseur et al. 2020). Here $S = 1$ is the monodisperse end member and $S = 0$ is infinitely polydisperse. It is useful to compute S and, for distributions $S < 1$, to account for the polydispersivity in diffusion scaling. This is not necessary when concentration gradients are measured within individual particles, but it is necessary when we are using bulk metrics, such as the total leached amount of a diffusing species in a population of particles of different sizes.

In monodisperse populations of spheres where there is a defined single R, $\lambda_{\mathcal{D}}$ is defined as described above. However, for polydisperse distributions of spheres, there is not a single R. This has two effects, first, it means that any bulk signal, such as the bulk amount of extraction of calcium from a distribution of spheres requires a weighted scaling, and second, $\lambda_{\mathcal{D}}$ needs redefining.

First, $\langle \bar{C} \rangle$ can be weighted as a function of the probability density function of the particle size distribution $F(R)$. The result of such a weighting, which we call $\langle \bar{\bar{C}} \rangle$, can be found by

$$\langle \bar{\bar{C}} \rangle = \int_0^\infty F(R) \langle \bar{C} \rangle \, dR \qquad \text{Eq. 10}$$

The value $\langle \bar{\bar{C}} \rangle$ then gives a bulk average concentration signal for a population of spherical particles of any distribution of radii. Radii data are more commonly cast as discrete binned measured data and not as a continuous function, in which case

$$\langle \bar{\bar{C}} \rangle = \sum_{j=1}^{j=n} \phi(R_j) \langle \bar{C} \rangle_j \qquad \text{Eq. 11}$$

where $\langle \bar{C} \rangle_j$ and R_j are the jth bin of $\langle \bar{C} \rangle$ and R, respectively, and ϕ is the volume fraction of the jth bin of R. In the definition of $\lambda_{\mathcal{D}}$, we take the characteristic lengthscale as $\langle R^3 \rangle^2 / \langle R^2 \rangle^2$ giving $\lambda_{\mathcal{D}} = \langle R \rangle^2 / [S \langle \mathcal{D} \rangle]$.

3. Materials and methods

We use the published results of experiments from Casas et al. (2019) in which rhyolitic glass particles are exposed to hot SO_2 gas. In this section, we document how the experimental material was prepared, the conditions of the experiments, and the analysis of the experimental products undertaken.

a. Preparation of experimental material

To test how diffusion of calcium evolves in distributions of particles exposed to a gas phase, we re-analyze a suite of data presented in Casas et al. (2019). For completeness, we repeat the experimental details here. The data were produced using a natural rhyolitic obsidian from Hrafntinnuhryggur, Krafla (Iceland), the source location for which is described in detail in Tuffen and Castro (2009). Specifically, the material was collected from the approximate AO locality given in Tuffen and Castro (2009) and which has a bulk composition given in Table 1, measured using milled powder of the same material by electron microprobe spot analyses (Ludwig-Maximilians-Universität). For the electron microprobe analysis, we used a Cameca SX-100 with LaB6 cathode and five spectrometers; measurement conditions were 10 μm diameter defocused beam at 5 nA and acceleration voltage of 15 kV. For all elements, peak and background measurement times were 10 and 5 s, respectively.

As described in Casas et al. (2019), the sample was crushed gently into powder using a Retsch GmbH centrifugal ball mill S1000 under dry conditions at rates sufficiently slow to ensure that no appreciable heating occurred. The material was then sieved to achieve three distinct particle size distributions confirmed using a Beckman-Coulter LS230 laser particle diffraction analyzer. The particle size distributions are given in Fig. 2. Throughout this contribution, we refer to these three size distribution samples by the mean radius $\langle R \rangle$, such that the distributions are $\langle R \rangle = 10.6$ μm, $\langle R \rangle = 19.5$ μm, and $\langle R \rangle = 127.7$ μm (Fig. 2).

b. Gas-ash reaction experiments and reaction products

The powder samples were loaded into the gas-solid reactor described in Ayris et al. (2015). This reactor is composed of a hand-blown quartz glass (SiO_2) tube with a sample bulb at one end, and open at both ends. The sample is placed in the bulb which has internal paddles that keep the sample in motion as the bulb and tube rotate. The tube sits in the central hot zone of a 3-zone furnace in which temperature is monitored by a K-type thermocouple accurate to within ± 2 K. Once the sample powder is heated to an isothermal working temperature, an SO_2-Ar mixture for which 1 mol.% is SO_2 and 99 mol.% is Ar, is pumped into the furnace and into the glass tube at a constant volumetric flow rate, regulated by flow controllers. While Casas et al. (2019) produce and analyze a larger dataset using other gas mixtures (e.g. SO_2+H_2O), we focus on the SO_2-Ar experiments. The pre- and post-experimental sample surfaces were analysed using a Hitachi field-emission scanning electron microscope SU5000.

c. Bulk leachate data collection and treatment

After each experiment, the samples were taken out of the reactor and left to cool to room temperature. The collected samples were stored in vials. We leached the samples with deionized water for 1 h at a 1/250 solid/water ratio, followed by filtration through 0.22 μm mixed cellulose ester membrane. Ion analysis were performed with a Metrohm Ion Chromatography system (733 separation center and 732 conductivity detector). This method results in a measurement of the composition of any surface compounds that can be dissolved, such as salts of interest here. Leaching of components from the underlying glass is negligible at these conditions. This allowed the measurement of calcium ion (Ca^{2+})

concentration as a function of time and temperature of exposure to SO_2. The value of Ca^{2+} is recorded as a mass fraction of the total mass of the sample. For high temperature volcanic particles in the presence of SO_2 gas, this leachable component has been shown to be the Ca^{2+} that diffused to the surface sites of the particles and formed solid $CaSO_4$ crystals, which dissolve in the deionized water (Ayris et al. 2013). The average initial calcium concentration in the obsidian is 1.66 ± 0.04 wt.% as CaO, or 1.19 ± 0.04 wt.% as Ca (Table 1), which provides a reference value for use in our analysis.

The values of Ca^{2+} concentration leached by our analysis represent the total amount of calcium that has been removed from the rhyolitic glass and deposited on the surface as salts, which we can call C_T. Therefore, taking C_r to be the initial amount, we can define $\langle \bar{\bar{C}} \rangle = C_r - C_T$ as the concentration remaining in the glass. In Fig. 3 we report the values of C_T relative to C_r, which we term $\bar{C}_T$. The data demonstrate that the evolution of $\bar{C}_T$ is non-linearly dependent on time of exposure to SO_2 gas, and is also dependent on the temperature and the particle size distribution (Ayris et al. 2013; Casas et al. 2019).

We convert t into $\bar{t}$ using several different methods, rendering the data of $\bar{C}_T$ a function of dimensionless time. Then we compare these methods with model results for the process. We note that for any of the results using Eq. 3, $\bar{C}_T = 1 - \langle \bar{C} \rangle$, for the monodisperse case, or, additionally when using Eq. 11, $\bar{C}_T = 1 - \langle \bar{\bar{C}} \rangle$ for the polydisperse case. In Fig. 4, we present the monodisperse solution for $\bar{C}_T = 1 - \langle \bar{C} \rangle$ and the polydisperse solution for $\bar{C}_T = 1 - \langle \bar{\bar{C}} \rangle$ for each of the three particle size distributions given in Fig. 2. Using the non-dimensionalization of time we describe for diffusion in monodisperse spheres, the solution is universal and invariant of the conditions used. Using the non-dimensionalization of time we describe for diffusion in polydisperse spheres, there is not a unique collapse of the model curves for arbitrary size distribution, although the solution can be computed for any size distribution required.

d. Iron oxidation state

The bulk iron oxidation state was measured by positive analysis for FeO wt.% using potentiometric titration based on the method described by Shapiro and Brannock (1956). Using potassium dichromate ($K_2Cr_2O_7$) 0.01 N as titrant solution, a 665 Metrohm Titroprocessor, a 685 Dosimat automatic titrator connected to an E 649 Magnetic Swing-out Stirrer with an electrode holder and a platinum reference (silver-silver chloride) electrode. The Fe_2O_3 content was determined by difference between wet chemically determined FeO and total Fe from electron microprobe analyses (see below). The initial oxidation state of the iron in the sample was measured using a titration method to be 0.153 Fe^{3+}/Fe_T (Casas et al. 2019).

e. Electron microprobe analysis of spatial gradients of calcium profiles

For a subset of the experimental samples, we took the resultant post-experimental SO_2-treated glass particles and mounted them in a layer 1-particle deep in resin before polishing them to a depth where the exposed particle cross sections were approximately at a depth such that the particle centres were visible (i.e. to a depth of 1 particle radius). The polished particle sections were analyzed using a Cameca SX100 electron microprobe with a 15 kV accelerating voltage, 15 nA beam current, and a defocused 3-10 μm spot size and ZAF correction procedures. Analyses were performed over 10 s with 5 s background measurements. To check for homogeneity and consistency, at least 10 measurements were made at each spot. We measured transects across the particles to check for gradients in particular elements.

4. Results and analysis

We interpret the leached concentrations of Ca^{2+} to be derived exclusively from the soluble salt compounds on the particle surfaces, and not to represent any significant component of calcium derived from the glass itself post-experiment. Here we describe and interpret these experimental results. In this section we assume that $\mathrm{Bi} \gg 1$, such that we use Eq. 8a, rather than Eq. 8b at the particle rim when solving our diffusion model.

In this section, we present the experimental data from Figure 3 in dimensionless space. This has the effect that for the monodisperse models (using Eq. 3), there exists a single universal model solution (black curves in Fig. 4), and the data are normalized to compare with this model by fitting for the diffusivity (see below). The same is true for the polydisperse models except that due to our specific choice of normalization (Section 2), there is no single model solution, and subtle differences exist for each model solution for each specific shape of particle size distribution (Fig. 4).

a. Analysis of data using a diffusivity dependent only on temperature

We can normalize the data assuming that the diffusivity $\mathcal{D}$ is a function of temperature only and is not dependent on concentration. To do this, we minimize for the best fit $\mathcal{D}$ that describes a given time-series of data at a given temperature using a least squares fitting algorithm. This results in the best fit $\mathcal{D}$ for each temperature and for each particle size distribution. In Fig. 4a we demonstrate that this fitting results in a good collapse of the data and to the monodisperse solution given by Eq. 3 regardless of polydispersivity, and that the global coefficient of determination is 0.90. For this approach, the time-series data is normalized by $\bar{t} = t/\lambda_{\mathcal{D}} = \mathcal{D}t/R^2$ as described in §2b. In Fig. 4b we show that the effect of polydispersivity can be extracted when compared with Eq. 3 solved with the weighting in Eq. 11, where the global coefficient of determination is 0.94. In this approach, the time-series data are normalized by $\bar{t} = t/\lambda_{\mathcal{D}} = S^2\langle\mathcal{D}\rangle t/\langle R\rangle^2$ as described in §2e. The inset to Fig. 4b gives the individual collapses for each particle size distribution compared with the weighted models. This fitting procedure results in a given value of $\mathcal{D}$ for each T given in Table 2.

b. Analysis of data using a concentration- and temperature-dependent diffusivity

Here we normalize the data assuming the diffusivity $\mathcal{D}$ is a function of both temperature and the local concentration of calcium and that this dependence has the form given in Eq. 7. A virtue of our choice of non-dimensionalization is that we can globally fit the data for a given β and $\mathcal{D}_\beta$ (or equivalently for γ and $\mathcal{D}_\gamma$) in our definition of $\mathcal{D}_r$. When we adjust these parameters, we find excellent agreement in all cases.

First, we focus on the dependence of $\mathcal{D}$ on concentration given in Eq. 7b, which is a linear dependence. When we apply this global fitting procedure in the monodisperse model solving for Eq. 3 with Eq. 7b, we find a universal collapse of all data for all temperatures and particle size distributions to the model $1 - \langle\bar{C}\rangle$ with a coefficient of determination of 0.95 (Fig. 4c). This approach uses the normalization of time given by $\bar{t} = t/\lambda_{\mathcal{D}} = \langle\mathcal{D}\rangle t/R^2$ for all data where $\langle\mathcal{D}\rangle$ is computed from the model. Second, when we apply this fitting procedure using the polydisperse model solving Eq. 3 with Eq. 7b, weighted using Eq. 11, we also find a general collapse of each particle size distribution to the respective model result for $1 - \langle\bar{\bar{C}}\rangle$ with a coefficient of determination of 0.94 (Fig. 4d). This approach uses the normalization of time given by $\bar{t} = t/\lambda_{\mathcal{D}} = S\langle\mathcal{D}\rangle t/\langle R\rangle^2$ for all data where, again, $\langle\mathcal{D}\rangle$ is computed from the model. This provides a globally fitted β and $\mathcal{D}_\beta$ for both monodisperse and polydisperse conditions (Table 2).

When fitting using the exponential form of $\mathcal{D}(T, C)$ via Eq. 7c and minimizing for $\mathcal{D}_\gamma$ and γ, we find a comparable coefficient of determination as given above for the linear dependence of $\mathcal{D}(T, C)$. However, the similarity in coefficient of determination imply that we do not have statistical grounds on which to invoke an exponential form of $\mathcal{D}(T, C)$ and is therefore not shown here graphically. Nevertheless, these results are given in Table 2.

5. Discussion

a. Diffusivity of calcium in rhyolite

Using different techniques to fit for the diffusivity of calcium as a function of (1) temperature or (2) temperature and concentration, results in values or relationships that we can compare with previously published data. We collate published values of $\mathcal{D}(T)$ computed from experimental data for diffusion of calcium in rhyolitic materials (Jambon 1982; van der Laan et al. 1994; Mungall et al. 1999) as well as an indirect estimation of calcium diffusivity from experiments performed in a similar manner as those presented here (Ayris et al. 2013).

In Fig. 5 we show how the fitted diffusivities arising from the approach described in §4 compare with published diffusivities. When we use Eq. 7a defining a temperature dependence of $\mathcal{D}$ only, we have a single fit diffusivity for each temperature and each particle size distribution. In Fig. 5a & 5b we show the fitted $\mathcal{D}(T)$ using the monodisperse solution (Fig. 5a) and the polydisperse solution (Fig. 5b). For a given experimental temperature the diffusivities agree relatively well regardless of particle size or particle size distribution. When we use Eq. 7b defining both temperature and a concentration dependence of $\mathcal{D}$, we have a global Arrhenius fit for each particle size distribution used, rather than individual results for each temperature (see Fig. 5c & 5d). In Fig. 5c, we make the arbitrary choice to show the fit result for $C = C_r$, that is, for when the calcium concentration is at its initial value. Whereas in Fig. 5d, we show the single, universal, polydisperse solution with a direct mapping for the local calcium concentration. In all cases shown in Fig. 5, it is clear that the slope of our $\mathcal{D}(T)$ results differ from previous work shown (Fig. 5), which would relate to an apparent difference in activation energy of the calcium diffusion process. Our shallow temperature dependence relates to a lower activation energy for diffusive mass transport in our case than in previous cases. Mungall et al. (1999) finds that the activation energy is $E = 248$ kJ.mol^{-1}. In contrast, we find a good description of our data using a constant $E = 153$ kJ.mol^{-1}, independent of the concentration of calcium (e.g. Fig. 5b). This discrepancy warrants investigation.

In liquid systems, the relationship between $\mathcal{D}$ and T has been proposed to relate simply to a relationship between the liquid viscosity μ and T (Glasstone et al. 1941). The so-called Eyring diffusivity $\mathcal{D}_{\mathrm{E}}$ is given by

$$\mathcal{D}_{\mathrm{E}} = \frac{k_B T}{l\mu} \qquad \text{Eq. 12}$$

where k_B is Boltmann's constant, and l is an effective jump distance of a given diffusing component. The most appropriate diffusing component to associate with the viscosity is oxygen diffusion, with a jump distance of the order of 0.1-1 nm. Specific estimates have been made of $l = 0.5$ nm (Dingwell 1990; Mungall 2002) or as low as $l = 0.14$ nm (Watkins et al. 2009).

We use a rhyolite viscosity model from Hess and Dingwell (1996) with an initial concentration of dissolved water of 0.14 wt.% (Tuffen and Castro 2009) in order to compute μ for each experimental temperature used here. We then use a subset of the published data for $\mathcal{D}(\mu)$ for calcium diffusion in rhyolite, for which constraint of $\mu(T)$ was given (Mungall et al. 1999; Watkins et al. 2009; Ayris et al. 2013). Taken together, this allows us to re-plot the $\mathcal{D}(T)$ results from Fig. 5 in terms of $\mathcal{D}(\mu)$, along with Eq. 12 (Fig. 6).

In Fig. 6, we show that our model results for $\mathcal{D}(T, C)$ are broadly consistent with previous results for calcium diffusivity in rhyolites when examined as $\mathcal{D}(\mu)$. Our model is constrained at a high range of μ (low-temperature), compared with previous results (Fig. 6a). Extrapolation of our model (Fig. 6b) encapsulates the previous data captured at higher relative μ. This leads us to conclude that both the Watkins et al. (2009) and the Mungall et al. (1999) data straddle the transition from the so-called

'intrinsic diffusion' regime to the 'extrinsic diffusion' regime, as defined by Dingwell (1990). At high temperatures, or low viscosities, calcium diffuses in rhyolite particles proportional to Eq. 12, while at low temperatures, or high viscosities, calcium diffuses more quickly than would be predicted by Eq. 12.

A concentration dependence of $\mathcal{D}$ for calcium in rhyolite reported here potentially further explains some of the differences between the values of $\mathcal{D}$ reported in the literature even for experimental work performed in the same region of T. For example, Jambon (1982), Van der Laan et al. (1994), and Mungall et al. (1999) all provide data for $\mathcal{D}$ for calcium in rhyolitic liquids at similar temperatures (or viscosities), and yet their values differ. While this may possibly be ascribed to analytical uncertainty in their methods or to technical differences in experimental design, it is striking to note that the slightly elevated $\mathcal{D}(T)$ values found by Jambon (1982) and Van der Laan et al. (1994) relative to those found by Mungall et al. (1999) in the same range of temperatures, could be ascribed to the fact that the initial concentration of calcium in the starting materials was higher in Jambon (1982) and Van der Laan et al. (1994) compared with the trace quantities synthesized in Mungall et al. (1999). We note a positive dependence of $\mathcal{D}(T)$ on C in our work and, although this dependence is spatially variable as diffusion progresses, it is true that high bulk C_i would result in higher average measured $\langle\mathcal{D}\rangle(T)$.

b. Diffusion mechanisms and charge compensation by local iron oxidation

Casas et al. (2019) showed that Na^+ and K^+ are mobile in addition to Ca^{2+}, feeding the formation of sodium- and potassium-sulfate at the particle surfaces. On the basis that the calcium sulfate is the dominant salt formed, we have neglected the motion of these cations in our model development. Nevertheless, their mobility, however slight, raises the question whether or not multicomponent diffusion of cations affects the motion of calcium. The analysis given in Fig. 6 suggests that casting diffusivities as a function of the material property viscosity effectively explains subtle differences in the temperature-dependence of calcium diffusivity associated with small differences in base rhyolite composition. This has the same effect as the approach taken by Renggli et al. (2019) who normalized temperatures by the glass transition temperature for each composition considered. This approach also suggests that small changes in viscosity associated with the removal of calcium or other cations from the glass may influence the diffusivity of calcium; effectively rendering this a multi-component diffusion problem. To test this, we use a multicomponent viscosity model (Giordano et al. 2008) to confirm that the extraction of calcium and other cations have a negligible effect on viscosity (see sub-vertical temperature-dependent curves in Fig. 6b), and therefore, we conclude that it is likely that calcium is effectively moving independently in this rhyolitic composition. This is further consistent with the initially high proportion of excess network-modifying cations (see Table 1), which are not depleted by the SO_2 reaction.

The experiments analyzed here show that in the presence of SO_2 gas, rhyolite particles will form calcium sulfate crystals on their surfaces. The analysis of the leachate data interrogated above then confirms that this is rate-limited by the diffusion of calcium from the bulk of the rhyolite particle toward the surfaces (e.g. Ayris et al. 2013). Conservation of charge neutrality in the melt implies the movement of calcium out of the particles must be compensated. Following Cook and Cooper (2000), we hypothesize that the observed extraction of Ca^{2+} is compensated by the local oxidation of iron $Fe^{2+} \rightarrow Fe^{3+}$. The iron oxidation would be stabilized by monovalent cations Na^+ and K^+ if Fe^{3+} then takes a tetrahedral network-forming role (Dickenson and Hess 1986).

The above suggests that the SO_2-rhyolite reaction is accompanied by an inward-moving auto-oxidation front in the particles that proceeds at the same rate as the diffusion of calcium outward, and limited by the diffusivity of calcium out rather than the diffusivity of any oxidizing agent moving inward (Cook and Cooper 2000). We test this hypothesis directly by confirming that while the initial Fe^{3+}/Fe_T state of the particles of rhyolite was 0.153, the oxidation state of the particles after 1 hour exposure to SO_2 at 800 °C, this value increased to 0.318. In Fig. 7 we show that the mol. fraction of calcium leached

from the surface deposits is linearly inversely proportional to the mol. fraction of Fe^{3+}, which is consistent with this charge compensation mechanism.

The auto-oxidation of iron to accommodate the flux of calcium out of the particles allows us to place the experimental results analyzed here in the wider context of rhyolites worldwide. For example, we hypothesize this process is therefore limited by both the total Ca^{2+} and Fe^{2+} available initially in the ash particles. Taking a global database of rhyolite glass compositions (Di Genova et al. 2017), we see that the rhyolite used here has more initial total iron and calcium than the mean of natural rhyolite glasses worldwide (Fig. 8). We suggest that it may be high-iron (specifically high reduced iron), high-calcium rhyolites that will be most susceptible to SO_2-ash reactions after fragmentation.

c. The importance of surface reaction rates

As a final test of our model, we apply it directly and without fitting to the spatial distribution of calcium measured in an experimental run product, by using an electron microprobe method (see Section 3). In this case the monodisperse model is sufficient because the particle radius is measured directly.

In Fig. 9 we show a typical transect of calcium measured as CaO (wt.%). Running our model with the constraints from the leachate data as inputs, and using the measured R for the particles in question, we find reasonable agreement for $C(r)$ (Fig. 9). These data imply that the value of CaO close to the boundary of the particles does indeed fall to low values consistent with $C_x \approx 0$, which implies $\mathrm{Bi} \gg 1$. Moreover, this suggests that the boundary reaction rate is not rate-limiting. If we relax this assumption and fit for H in the solution to Eq. 3 applied to the data in Fig. 9, we find that $H = 1.96 \times 10^{-9}$ m.s^{-1}, consistent with $\mathrm{Bi} = 4.02$. This is in the condition $\mathrm{Bi} > 1$, confirming that the reaction at the surface is not rate-limiting. To a first order, this confirms that the kinetics of the particle surface reaction can be neglected and that the process is dominantly rate limited by the motion of calcium from the bulk to the surface by diffusion.

Casas et al. (2019) found no textural evidence that the surface of the particles became coated or 'armored' by sulfate deposits in these tumbling experiments. However, presumably longer duration experiments without tumbling would result in complete surface coverage, which has been shown to induce a change in dynamics (Renggli and King 2017). Surface coverage would presumably occur at longer experimental timescales, and/or if more initial calcium were available to feed continued reaction.

6. Implications

Our model solves the particle-scale kinetics of SO_2-particle reactions in volcanic environments, and is motivated by evidence for sulfate salts on fresh volcanic ash (Rose 1977; Varekamp et al. 1984; Gerlach and McGee 1994; De Hoog et al. 2001; de Moor et al. 2005), which could be evidence for SO_2 scrubbing in volcanic conduits or plumes (Ayris et al. 2013; Delmelle et al. 2018). Here, we consider a few principal applications for this model.

Our kinetic model could be coupled with existing conduit (Degruyter et al. 2012) or volcanic plume models (Costa et al. 2016), to predict the total mass of SO_2 scrubbed in a given eruption. Simple calculations already suggest that the scrubbed quantity could be significant (Ayris et al. 2013) and that scrubbing may be similarly important for other gases such as HCl (Ayris et al. 2014). However, these predictions are based on a model that iterates a simplified diffusion calculation for either isothermal conditions, or for average temperature-time pathways in volcanic plumes (Ayris et al. 2013, 2014), and all for monodisperse particles of a given representative size. In full 3D plume simulations, the velocity and temperature field vary strongly in time and space (Costa et al. 2016), and in volcanic conduits, particle-particle interactions may modify the particle size distribution dynamically (Dufek et al. 2012). These complexities can be accounted for by the model presented herein, which can be coupled to models that predict the evolution of the particle size distribution and temperature in time and space, and therefore may be used to make improved predictions of the scrubbing potential of eruptions of different magnitudes.

The model we present and validate herein is a particle-scale model. Solving a particle-scale diffusion model for particles in an evolving plume or conduit flow model would be computationally expensive, if not infeasible. Therefore, in our model, we specifically additionally validate a polydisperse model in which the bulk response of an ensemble of reacting particles can be determined, if the distribution of particle sizes is known. This strength of our polydisperse model would allow it to be coupled to plume models without the need to solve individual particle-scale dynamics and to instead take a volume-averaged approach for each spatial node, rendering the problem computationally tractable.

There is a well-documented mismatch between observed atmospheric loading of SO_2 from a given eruption, and the petrological estimate of the sulfur budget from the same magma volume involved in the eruption (Shinohara 2008; Edmonds et al. 2010; Wallace and Edmonds 2011). For silicic eruptions, this mismatch has been resolved by invoking an additional source of sulfur from the crust – e.g. degassed sulfur provided by deeper mafic magmas (Edmonds et al. 2010). Once a total scrubbing potential of a given eruption was predicted using our model in conjunction with a 3D plume model, that would have direct implications for these kinds of mass-balance calculations from which the volumes of mafic magma at depth are estimated (Wallace 2001). Therefore, we envisage that implications of a well-calibrated SO_2 scrubbing model are not only for atmospheric SO_2 loads, but also for crustal sulfur budgets. The nature of these particle-SO_2 reactions is such that it may represent a key missing reaction pathway in the volcanic sulfur cycle.

Future work could apply this model directly to estimate bulk SO2 scrubbing efficiency in volcanic conduits and in the hot core of volcanic plumes. This would require independent constraint of the temperature and velocity field to which the particles are exposed, but once known, our model is sufficiently flexible that the non-isothermal complex temperature-time pathway experienced by a batch of particles can be accommodated. The desirable output is a prediction of the bulk mass of SO_2 reacted in any closed system, that goes beyond the simple calculations that have been performed previously.

Acknowledgments

We are grateful to Elena Maters, Ed Llewellin, Antonio Costa, Mike James, and Madeleine Humphreys for stimulating discussion, to Penny King and 3 anonymous reviewers for feedback, and to Charles Lesher and Don Baker for editorial oversight and Daniel Neuville for editing the first submission in the same journal. We acknowledge funding from the European Research Council, ERC 2018 ADV Grant 834225 (EAVESDROP) and support from the Centre for Advanced Study in Munich, Germany.

Author contributions

F.B. Wadsworth, A.S. Casas, J. Vasseur, D.B. Dingwell and P.M. Ayris conceived and coordinated the work, A.S. Casas led the experimental campaign published elsewhere (Casas et al. 2019), J. Vasseur, K.-U. Hess, F.B. Wadsworth, and P. Delmelle analyzed the data. All authors contributed significantly to the manuscript.

References cited

Ayris, P.M., Lee, A.F., Wilson, K., Kueppers, U., Dingwell, D.B., and Delmelle, P. (2013) SO< sub> 2</sub> sequestration in large volcanic eruptions: High-temperature scavenging by tephra. Geochimica et cosmochimica acta, 110, 58–69.

Ayris, P.M., Delmelle, P., Cimarelli, C., Maters, E.C., Suzuki, Y.J., and Dingwell, D.B. (2014) HCl uptake by volcanic ash in the high temperature eruption plume: Mechanistic insights. Geochimica et Cosmochimica Acta, 144, 188–201.

Ayris, P.M., Cimarelli, C., Delmelle, P., Wadsworth, F.B., Vasseur, J., Suzuki, Y.J., and Dingwell, D.B. (2015) A novel apparatus for the simulation of eruptive gas-rock interactions. Bulletin of Volcanology, 77, 1–5.

Baldini, J.U.L., Brown, R.J., and McElwaine, J.N. (2015) Was millennial scale climate change during the Last Glacial triggered by explosive volcanism? Scientific Reports, 5.

Bluth, G.J.S., Rose, W.I., Sprod, I.E., and Krueger, A.J. (1997) Stratospheric loading of sulfur from explosive volcanic eruptions. Journal of Geology, 105, 671–683.

Burnett, D.S., Goreva, J., Epstein, S., Haldemann, S.L., Johnson, M.L., and Rice, A. (1997) SO2-rock interaction on Io 2. Interaction with pure so2. Journal of Geophysical Research E: Planets, 102, 19371–19382.

Carn, S.A., Fioletov, V.E., Mclinden, C.A., Li, C., and Krotkov, N.A. (2017) A decade of global volcanic SO2 emissions measured from space. Scientific Reports, 7, 1–12.

Casas, A.S., Wadsworth, F.B., Ayris, P.M., Delmelle, P., Vasseur, J., Cimarelli, C., and Dingwell, D.B. (2019) SO2 scrubbing during percolation through rhyolitic volcanic domes. Geochimica et Cosmochimica Acta.

Cook, G.B., and Cooper, R.F. (2000) Iron concentration and the physical processes of dynamic oxidation in an alkaline earth aluminosilicate glass. American Mineralogist, 85, 397–406.

Costa, A., Suzuki, Y., Cerminara, M., Devenish, B., Esposti Ongaro, T., Herzog, M., Van Eaton, A., Denby, L., Bursik, M., de' Michieli Vitturi, M., and others (2016) Results of the eruptive column model inter-comparison study. Journal of Volcanology and Geothermal Research, 326, 2–25.

Crank, J. (1975) The mathematics of diffusion, 415 p.

De Hoog, J.C.M., Koetsier, G.W., Bronto, S., Sriwana, T., and Van Bergen, M.J. (2001) Sulfur and chlorine degassing from primitive arc magmas: Temporal changes during the 1982-1983 eruptions of Galunggung (West Java, Indonesia). Journal of Volcanology and Geothermal Research, 108, 55–83.

de Moor, J.M., Fischer, T.P., Hilton, D.R., Hauri, E., Jaffe, L.A., and Camacho, J.T. (2005) Degassing at Anatahan volcano during the May 2003 eruption: Implications from petrology, ash leachates, and SO2 emissions. Journal of Volcanology and Geothermal Research, 146, 117–138.

Degruyter, W., Bachmann, O., Burgisser, A., and Manga, M. (2012) The effects of outgassing on the transition between effusive and explosive silicic eruptions. Earth and Planetary Science Letters, 349, 161–170.

Delmelle, P., Wadsworth, F.B., Maters, E.C., and Ayris, P.M. (2018) 8. High Temperature Reactions Between Gases and Ash Particles in Volcanic Eruption Plumes. In High Temperature Gas-Solid Reactions in Earth and Planetary Processes pp. 285–308.

Di Genova, D., Kolzenburg, S., Wiesmaier, S., Dallanave, E., Neuville, D.R., Hess, K.U., and Dingwell, D.B. (2017) A compositional tipping point governing the mobilization and eruption style of rhyolitic magma. Nature, 552, 235–238.

Dickenson, M.P., and Hess, P.C. (1986) The structural role and homogeneous redox equilibria of iron in peraluminous, metaluminous and peralkaline silicate melts. Contributions to Mineralogy and Petrology, 92, 207–217.

Dingwell, D. (1990) Effects of structural relaxation on cationic tracer diffusion in silicate melts. Chemical Geology.

Douglas, R.W., and Isard, J.O. (1949) The action of water and of sulphur dioxide on glass surfaces. J. Soc. Glass Technol, 33, 289–335.

Dufek, J., Manga, M., and Patel, A. (2012) Granular disruption during explosive volcanic eruptions. Nature Geoscience.

Edmonds, M., Aiuppa, A., Humphreys, M., Moretti, R., Giudice, G., Martin, R.S., Herd, R.A., and Christopher, T. (2010) Excess volatiles supplied by mingling of mafic magma at an andesite arc volcano. Geochemistry, Geophysics, Geosystems, 11, n/a-n/a.

Gerlach, T.M., and McGee, K.A. (1994) Total sulfur dioxide emissions and pre-eruption vapor-saturated magma at Mount St. Helens, 1980–88. Geophysical Research Letters, 21, 2833–2836.

Giordano, D., Russell, J.K., and Dingwell, D.B. (2008) Viscosity of magmatic liquids: a model. Earth and Planetary Science Letters, 271, 123–134.

Glasstone, S., Laidler, K., and Eyring, H. (1941) The theory of rate processes; the kinetics of chemical reactions, viscosity, diffusion and electrochemical phenomena.

Henley, R.W., King, P.L., Wykes, J.L., Renggli, C.J., Brink, F.J., Clark, D.A., and Troitzsch, U. (2015) Porphyry copper deposit formation by sub-volcanic sulphur dioxide flux and chemisorption. Nature Geoscience, 8, 210–215.

Hess, K.-U.U., and Dingwell, D.B. (1996) Viscosities of hydrous leucogranitic melts: A non-Arrhenian model. American Mineralogist, 81, 1297–1300.

Hsu, K.H. (1983) A Diffusion Model with a Concentration-Dependent Diffusion Coefficient for Describing Water Movement in Legumes During Soaking. Journal of Food Science, 48, 618–622.

Jambon, A. (1982) Tracer diffusion in granitic melts: experimental results for Na, K, Rb, Cs, Ca, Sr, Ba, Ce, Eu to 1300 C and a model of calculation. Journal of Geophysical Research: Solid Earth.

Johnson, M.L., and Burnett, D.S. (1993) SO2-rock interaction on Io: reaction under highly oxidizing conditions. Journal of Geophysical Research, 98, 1223–1230.

King, P.L., Wheeler, V.M., Renggli, C.J., Palm, A.B., Wilson, S.A., Harrison, A.L., Morgan, B., Nekvasil, H., Troitzsch, U., Mernagh, T., and others (2018, November 1) Gas-solid reactions: Theory, experiments and case studies relevant to earth and planetary processes. Reviews in Mineralogy and Geochemistry. Mineralogical Society of America.

Kueppers, U., Scheu, B., Spieler, O., and Dingwell, D.B. (2006) Fragmentation efficiency of explosive volcanic eruptions: A study of experimentally generated pyroclasts. Journal of Volcanology and Geothermal Research, 153, 125–135.

Mavrogenes, J., and Blundy, J. (2017a) Crustal sequestration of magmatic sulfur dioxide. Geology, 45,

705 211–214.

706 ——— (2017b) Crustal sequestration of magmatic sulphur dioxide as an ore-forming process. Applied
707 Earth Science, 126, 76–77.

708 Morioka, M. (1981) Cation diffusion in olivine-II. Ni-Mg, Mn-Mg, Mg and Ca. Geochimica et
709 Cosmochimica Acta, 45, 1573–1580.

710 Mungall, J. (2002) Empirical models relating viscosity and tracer diffusion in magmatic silicate melts.
711 Geochimica et Cosmochimica Acta.

712 Mungall, J., Dingwell, D., and Chaussidon, M. (1999) Chemical diffusivities of 18 trace elements in
713 granitoid melts. Geochimica et Cosmochimica.

714 Mysen, B., and Richet, P. (2005) Silicate Glasses and Melts, 544 p. Silicate Glasses and Melts.

715 Palm, A.B., King, P.L., Renggli, C.J., Hervig, R.L., Dalby, K.N., Herring, A., Mernagh, T.P., Eggins,
716 S.M., Troitzsch, U., Beeching, L., and others (2018) Unravelling the consequences of SO2-basalt
717 reactions for geochemical fractionation and mineral formation. Reviews in Mineralogy and
718 Geochemistry, 84, 257–283.

719 Renggli, C., and King, P. (2017) An experimental investigation of reactions between SO2 and
720 Anorthite-Diopside glasses.

721 Renggli, C.J., and King, P.L. (2018) SO2 Gas Reactions with Silicate Glasses. Reviews in Mineralogy
722 and Geochemistry, 84, 229–255.

723 Renggli, C.J., Palm, A.B., King, P.L., and Guagliardo, P. (2019) Implications of Reactions Between
724 SO2 and Basaltic Glasses for the Mineralogy of Planetary Crusts. Journal of Geophysical
725 Research: Planets, 124, 2563–2582.

726 Robock, A. (2000) Volcanic eruptions and climate. Reviews of Geophysics, 38, 191–219.

727 Rose, W.I. (1977) Scavenging of volcanic aerosol by ash: Atmospheric and volcanologic implications.
728 Geology, 5, 621–624.

729 Saadatfar, M., Brink, F., Latham, S., King, P., Middleton, J., Troitzsch, U., Turner, M., and Henley,
730 R.W. (2020) High resolution 3D mapping of grain kinematics during high temperature
731 sequestration of SO2 from flue gas by carbonate aggregates. Scientific Reports, 10, 2201.

732 Shapiro, L., and Brannock, W. (1956) Rapid analysis of silicate rocks.

733 Shinohara, H. (2008) Excess degassing from volcanoes and its role on eruptive and intrusive activity.
734 Reviews of Geophysics, 46.

735 Textor, C., Graf, H.F., Herzog, M., and Oberhuber, J.M. (2003) Injection of gases into the stratosphere
736 by explosive volcanic eruptions. Journal of Geophysical Research D: Atmospheres, 108.

737 Torquato, S. (2013) Random heterogeneous materials: microstructure and macroscopic properties, 701
738 p. Vol. 16. Springer Science & Business Media.

739 Tuffen, H., and Castro, J.M. (2009) The emplacement of an obsidian dyke through thin ice:
740 Hrafntinnuhryggur, Krafla Iceland. Journal of Volcanology and Geothermal Research, 185, 352–
741 366.

742 van der Laan, S., Zhang, Y., Kennedy, A.K., and Wyllie, P.J. (1994) Comparison of element and
743 isotope diffusion of K and Ca in multicomponent silicate melts. Earth and Planetary Science

744 Letters, 123, 155–166.

745 Varekamp, J.C., Luhr, J.F., and Prestegaard, K.L. (1984) The 1982 eruptions of El Chichón Volcano
746 (Chiapas, Mexico): Character of the eruptions, ash-fall deposits, and gasphase. Journal of
747 Volcanology and Geothermal Research, 23, 39–68.

748 Vasseur, J., Wadsworth, F.B., and Dingwell, D.B. (2020) Permeability of polydisperse magma foam.
749 Geology.

750 Wadsworth, F.B., Vasseur, J., Llewellin, E.W., and Dingwell, D.B. (2017a) Sintering of polydisperse
751 viscous droplets. Physical Review E, 95, 033114.

752 Wadsworth, F.B., Vasseur, J., Llewellin, E.W., Genareau, K., Cimarelli, C., and Dingwell, D.B.
753 (2017b) Size limits for rounding of volcanic ash particles heated by lightning. Journal of
754 Geophysical Research: Solid Earth, 122, 1977–1989.

755 Wallace, P.J. (2001) Volcanic SO2 emissions and the abundance and distribution of exsolved gas in
756 magma bodies. Journal of Volcanology and Geothermal Research, 108, 85–106.

757 Wallace, P.J., and Edmonds, M. (2011) The sulfur budget in magmas: Evidence from melt inclusions,
758 submarine glasses, and volcanic gas emissions. Reviews in Mineralogy and Geochemistry, 73,
759 215–246.

760 Watkins, J., DePaolo, D., and Huber, C. (2009) Liquid composition-dependence of calcium isotope
761 fractionation during diffusion in molten silicates. et Cosmochimica Acta.

762 Zhang, Y., and Cherniak, D.J. (2010) Diffusion in minerals and melts: Introduction. Reviews in
763 Mineralogy and Geochemistry, 72, 1–4.

764 Zhang, Y., and Ni, H. (2010) Diffusion of H, C, and O components in silicate melts. Reviews in
765 Mineralogy and Geochemistry, 72, 171–225.

766

767

768

769

Table 1 **The composition of the experimental material**

Oxide	From Tuffen & Castro (2009) n=100 [in wt.%]	This study using electron microprobe n=9 [in wt.%]	This study using electron microprobe n=9 [in re-normalized mol.%]
SiO_2	75.17 ± 0.41	75.20 ± 0.33	80.89 ± 0.39
TiO_2	0.22 ± 0.02	0.21 ± 0.04	0.17 ± 0.04
Al_2O_3	12.02 ± 0.16	12.06 ± 0.12	7.64 ± 0.08
FeO_T	3.13 ± 0.18	3.11 ± 0.11	2.37 ± 0.09
Fe_2O_3	-	0.88 ± 0.03	0.36 ± 0.01
FeO	-	2.23 ± 0.08	2.01 ± 0.08
MnO	0.11 ± 0.04	0.11 ± 0.04	0.10 ± 0.04
MgO	0.09 ± 0.02	0.08 ± 0.03	0.13 ± 0.05
CaO*	1.66 ± 0.10	1.66 ± 0.11	1.91 ± 0.14
Na_2O	4.58 ± 0.09	4.61 ± 0.08	4.81 ± 0.09
K_2O	2.88 ± 0.11	2.90 ± 0.09	1.99 ± 0.07
Total	99.86 ± 0.41	99.94 ± 0.50	100.0
Mol. fraction excess oxides**			0.032
NBO/T**			0.070

*The wt.% value of CaO from this study is taken as C_r

**Calculated using Mysen and Richet (2005)

770

771

772

This is the peer-reviewed, final accepted version for American Mineralogist, published by the Mineralogical Society of America.
The published version is subject to change. Cite as Authors (Year) Title. American Mineralogist, in press.
DOI: https://doi.org/10.2138/am-2021-7691. http://www.minsocam.org/
Resubmission: American Mineralogist

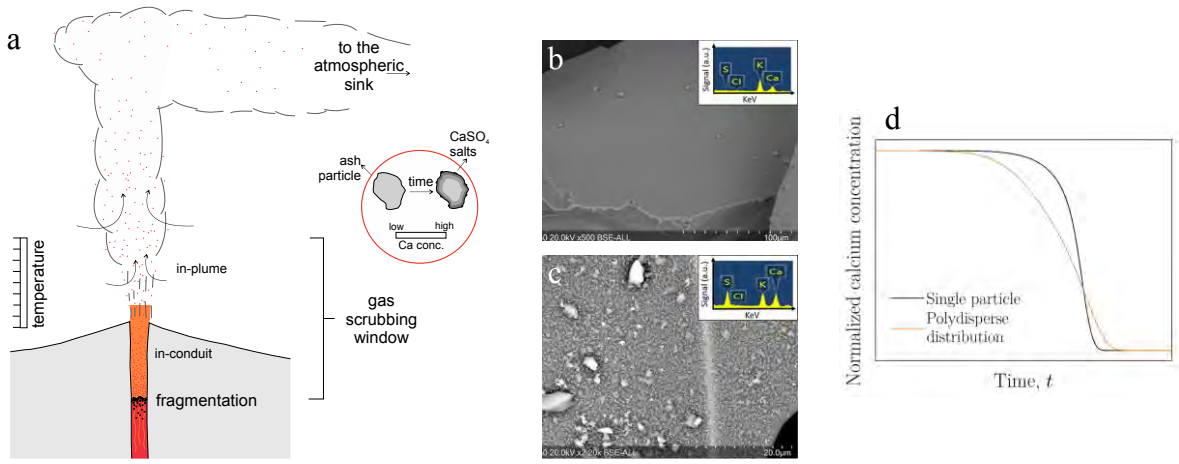

Figure 1.

The gas-particle reaction window in natural volcanic systems. (a) A cartoon of an eruption column cross section, showing the fragmentation level above which the gas, ash, and pyroclasts decouple and reactions can take place. *Inset:* A schematic of the particle-scale reaction described in Ayris et al. (2013) in which a particle exposed to SO_2 for time t at temperature T will form surface salts fed by cation diffusion toward the particle surface. (b-c) SEM images of the experimental products analysed here; (b) the starting material prior to treatment with SO_2, and (c) a surface of the experimental particle after exposure to SO_2 at 800 C for 1 hour. The images in panels (b) and (c) are reproduced from Casas et al. (2019) with permission. (d) A schematic view of the important different of a polydisperse compared with a monodisperse (or single particle) solution to Fickian diffusion.

This is the peer-reviewed, final accepted version for American Mineralogist, published by the Mineralogical Society of America.
The published version is subject to change. Cite as Authors (Year) Title. American Mineralogist, in press.
DOI: https://doi.org/10.2138/am-2021-7691. http://www.minsocam.org/

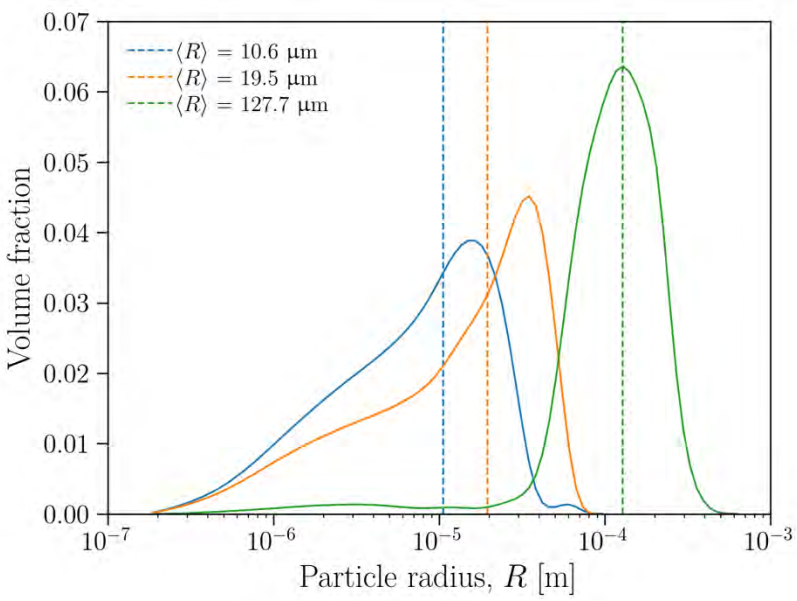

Figure 2.

The particle size distribution of the three populations of rhyolitic particles used in this study. Vertical dashed lines mark the arithmetic mean radius $\langle R \rangle$, which is also given on the figure as a numeric value.

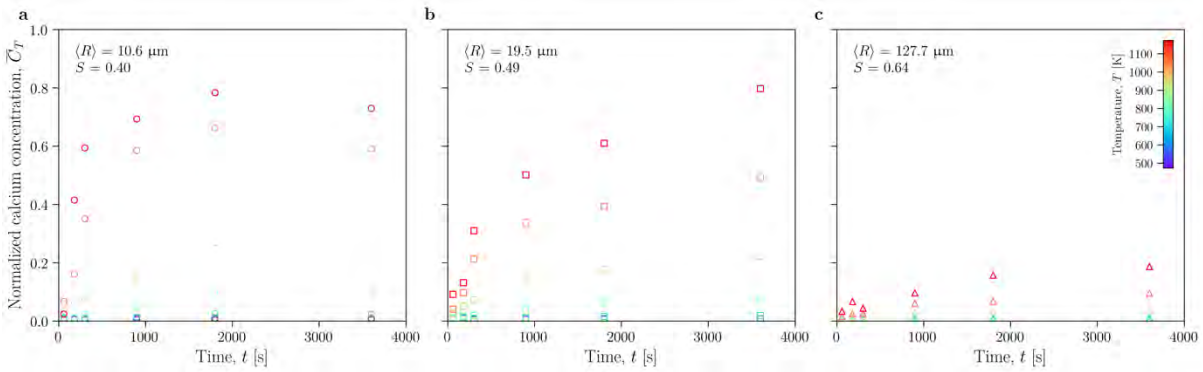

Figure 3.

Raw experimental results for calcium concentration leached from samples post-experiment normalized by the total calcium in the initial material, giving dimensionless $1 - \bar{C}_T$, as a function of the time of exposure to bypassing high temperature SO_2-Ar gas mixtures for each particle size distribution (a) $\langle R \rangle = 10.6$ µm, (b) $\langle R \rangle = 19.5$ µm, and (c) $\langle R \rangle = 127.7$ µm. Colors refer to temperature of exposure and labelled are the polydispersivity values S for each distribution.

This is the peer-reviewed, final accepted version for American Mineralogist, published by the Mineralogical Society of America.
The published version is subject to change. Cite as Authors (Year) Title. American Mineralogist, in press.
DOI: https://doi.org/10.2138/am-2021-7691. http://www.minsocam.org/
Resubmission: American Mineralogist

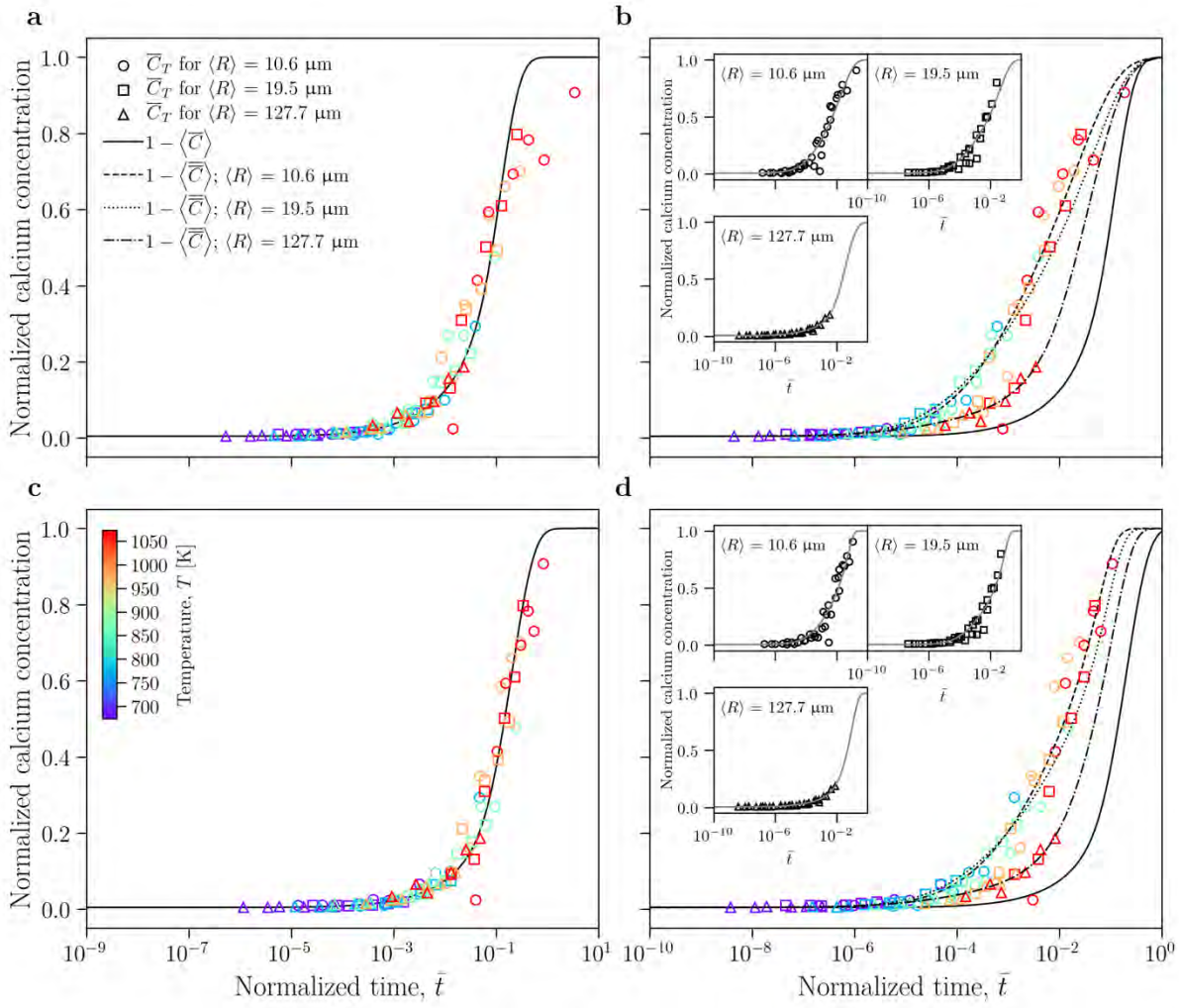

Figure 4.

The data presented in Fig. 3 where time t is transformed to dimensionless time $\bar{t}$ by $\bar{t} = t/\lambda_{\mathcal{D}}$ (see text). In panels (a) and (b) we show the comparison between the experimental data and our model for the case where the calcium diffusivity in $\lambda_{\mathcal{D}}$ depends only on temperature via Eq. 4 (or equivalently, via Eq. 7a). In this case the fit parameters are $\mathcal{D}_\alpha$ and α (see Table 2). In panels (c) and (d) we show the same comparison between the experimental data and our model, but for the case where the calcium diffusivity additionally depends on the local concentration of calcium via Eq. 5a (or equivalently, via Eq. 7b). In this case the fit parameters are $\mathcal{D}_\gamma$ and γ (see Table 3). In panels (a) and (c), we assume the particles are monodisperse with a size described by the mean particle size, whereas in panels (b) and (d), we use Eq. 11 to account for the particle size distribution polydispersivity (*insets:* the individual results for each particle size distribution).

This is the peer-reviewed, final accepted version for American Mineralogist, published by the Mineralogical Society of America.
The published version is subject to change. Cite as Authors (Year) Title. American Mineralogist, in press.
DOI: https://doi.org/10.2138/am-2021-7691. http://www.minsocam.org/
Resubmission: American Mineralogist

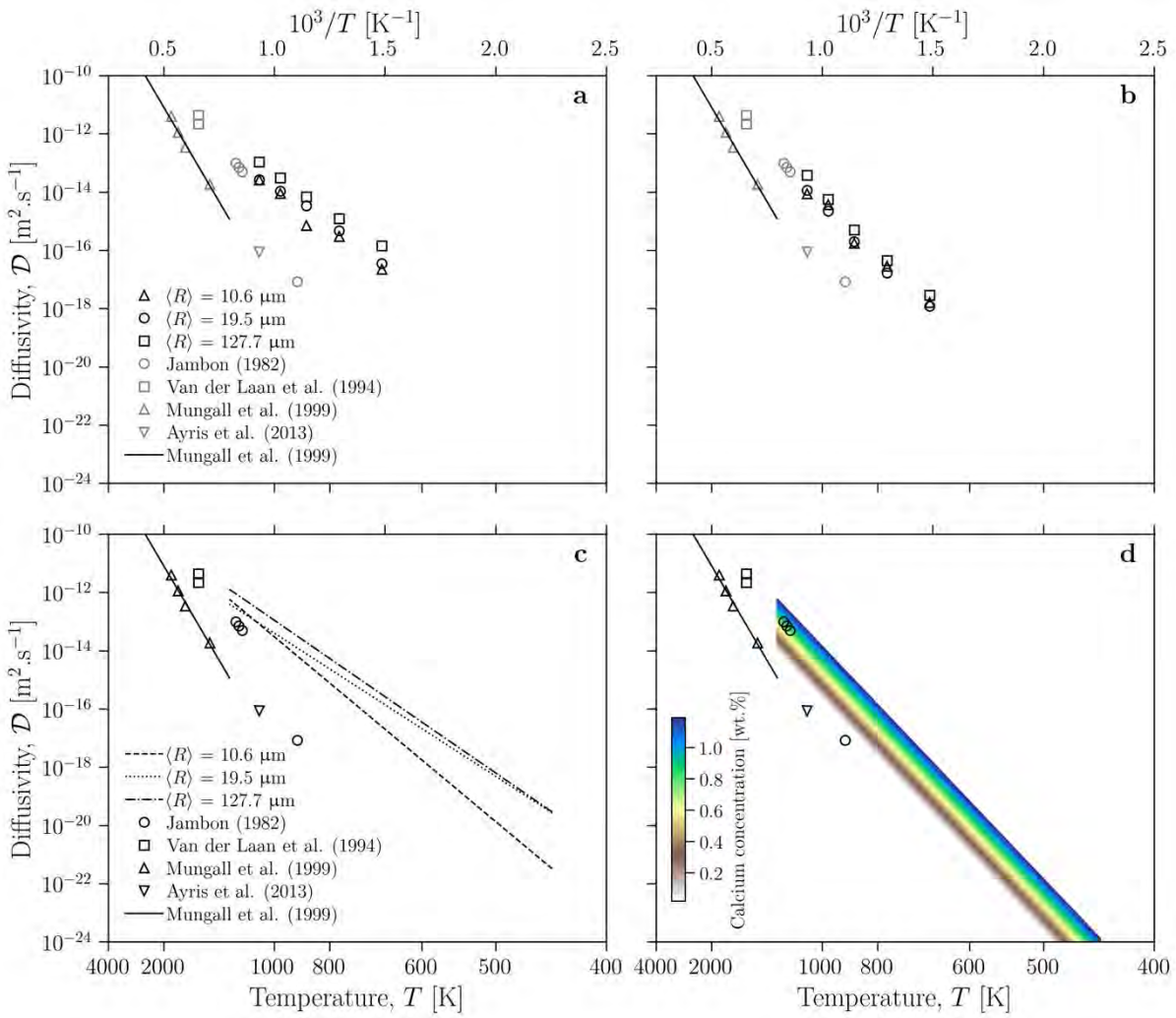

Figure 5.

The fitted calcium diffusivity as a function of temperature for the case where the diffusivity is temperature-dependent only – shown in (a) and (b) – and for the case where the diffusivity is dependent on both temperature and the local concentration of calcium – shown in (c) and (d). In panels (a) and (c), we assume the particles are monodisperse with a size described by the mean particle size, whereas in panels (b) and (d), we account for the particle size distribution polydispersivity.

This is the peer-reviewed, final accepted version for American Mineralogist, published by the Mineralogical Society of America.
The published version is subject to change. Cite as Authors (Year) Title. American Mineralogist, in press.
DOI: https://doi.org/10.2138/am-2021-7691. http://www.minsocam.org/
Resubmission: American Mineralogist

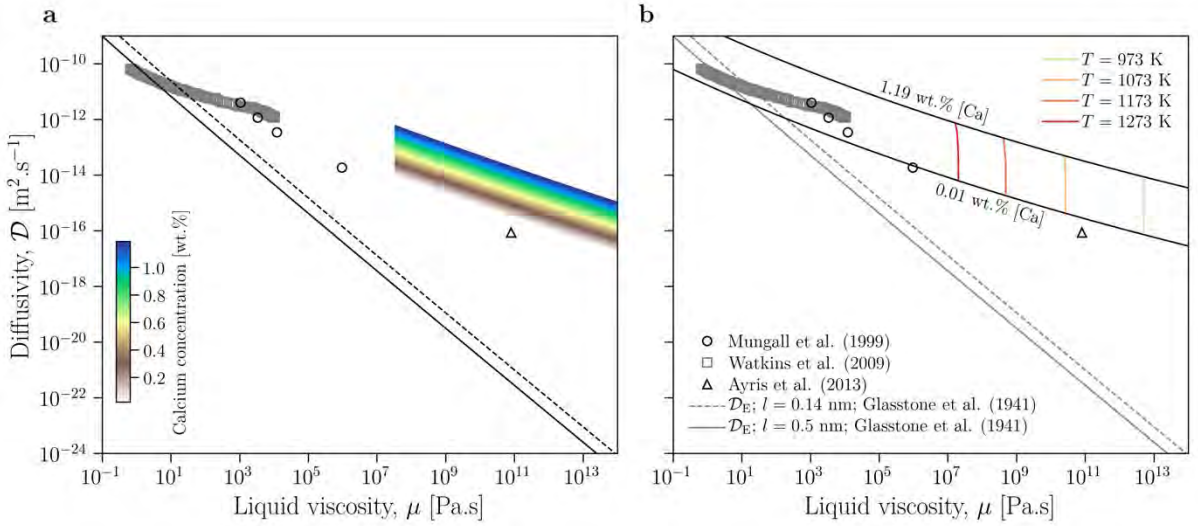

Figure 6.

The results shown in Fig. 5, but where T has been converted to μ, using either measured μ values for the materials used (i.e. in the case of Mungall et al. 1999), or calculated $\mu(T)$ values given by the model by Hess and Dingwell (1996), valid for rhyolites assuming nominally dry values of 0.06 wt.% total H_2O dissolved in the liquid (applied to the results of this study and to Ayris et al. 2013). In the case of Watkins et al. (2009), the values of μ are given directly. Additionally shown is the $\mathcal{D}_E(\mu)$ relationship Eq. 12, calculated for oxygen diffusivity using a jump-distance of either $l = 0.14$ or $l = 0.5$ nm. (a) Our model is given for a continuous range of calcium concentrations. (b) Our model is given for two different calcium concentrations and extrapolated to low-μ. The curves in (b) that are marked for temperature are the combined $\mathcal{D}$ and μ variation as particles lose calcium, showing that μ is not strongly affected by diffusive loss of calcium in this case (calculated using Giordano et al. 2008).

This is the peer-reviewed, final accepted version for American Mineralogist, published by the Mineralogical Society of America.
The published version is subject to change. Cite as Authors (Year) Title. American Mineralogist, in press.
DOI: https://doi.org/10.2138/am-2021-7691. http://www.minsocam.org/

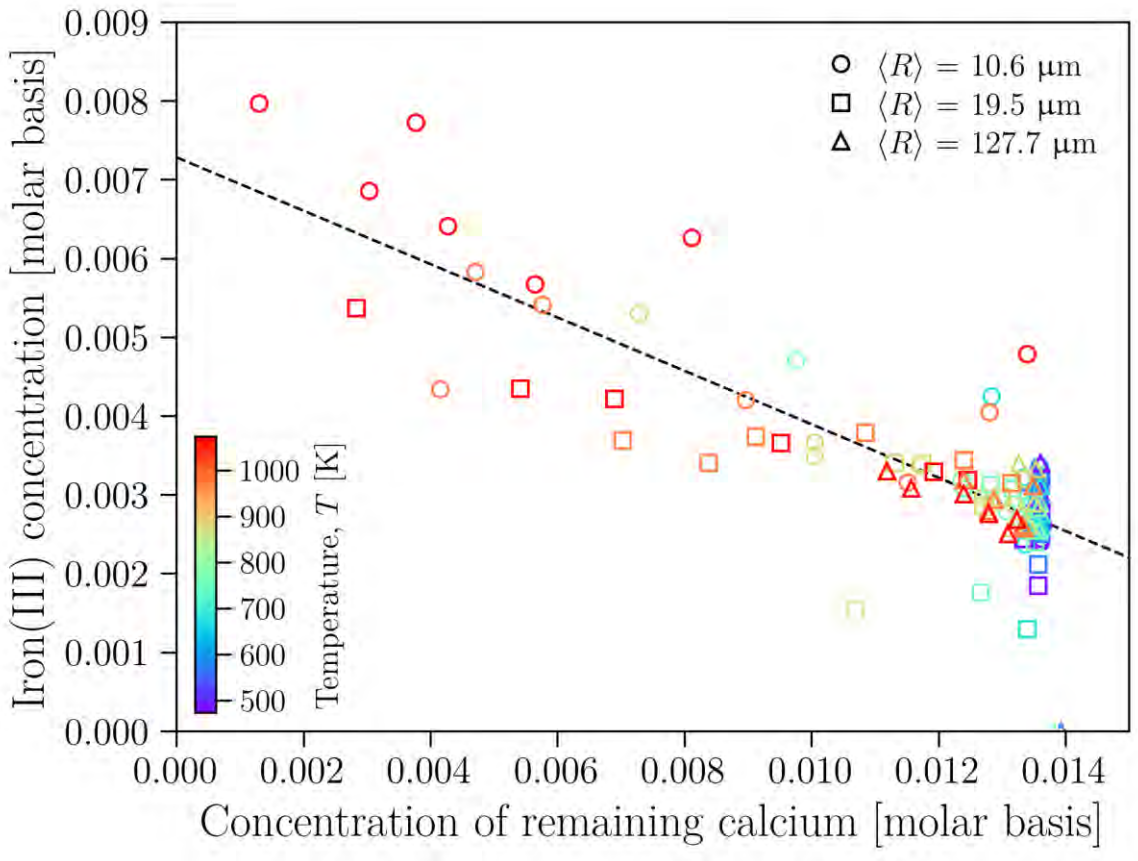

Figure 7.

The relationship between Fe^{3+} and C_T (both in mol. fraction and calculated on a single oxygen basis), showing a linear relationship for which the slope is approximately $-1/3$.

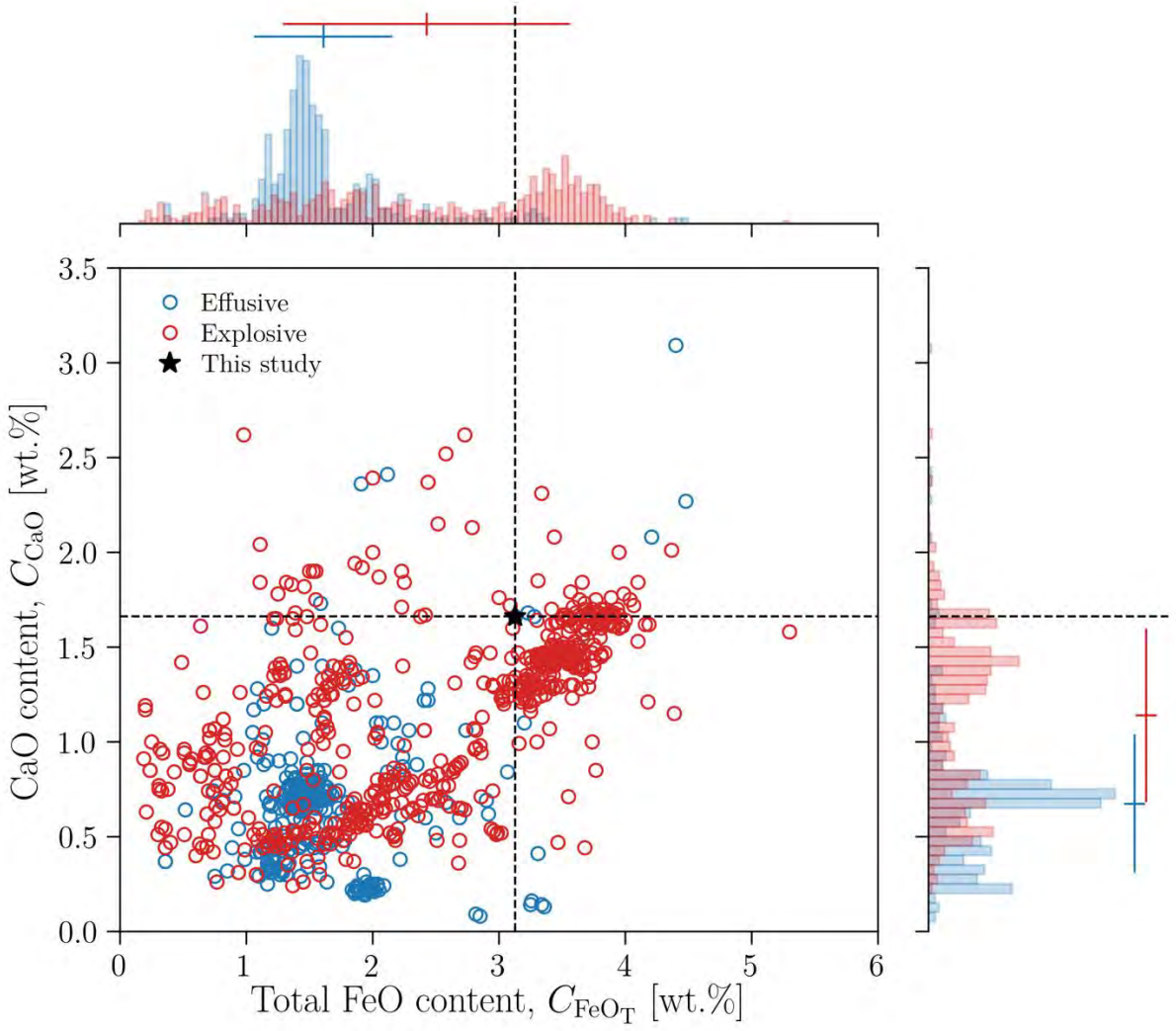

Figure 8.

CaO and FeO_T compositions of natural rhyolite glass worldwide (Using the composition database from Di Genova et al. 2017), divided into glass deposited from explosive or effusive eruptions. Here we note that it is the iron-rich, calcium-rich eruption products that are most susceptible to SO_2-ash reactions.

This is the peer-reviewed, final accepted version for American Mineralogist, published by the Mineralogical Society of America.
The published version is subject to change. Cite as Authors (Year) Title. American Mineralogist, in press.
DOI: https://doi.org/10.2138/am-2021-7691. http://www.minsocam.org/
Resubmission: American Mineralogist

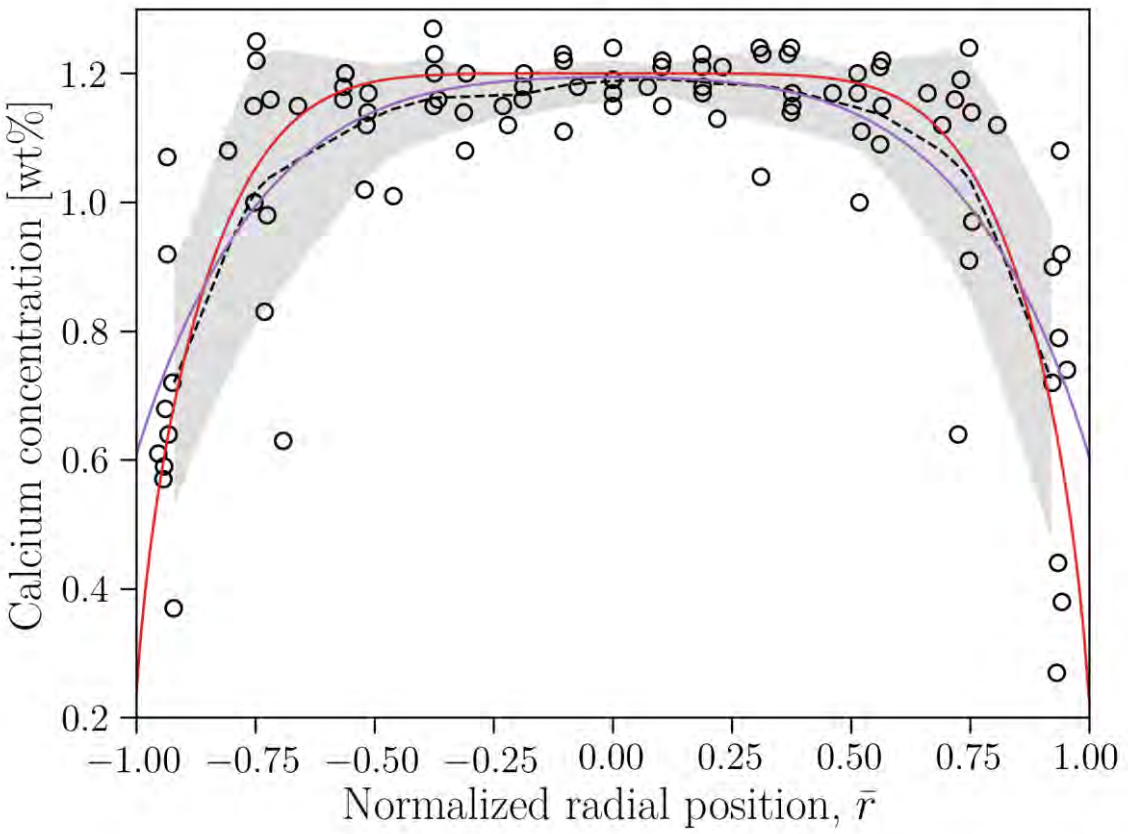

Figure 9.

Independent model verification using spatial gradients of calcium within rhyolite particles that have been exposed to SO_2 for 1 hour at 800 °C. Here $\langle R \rangle = 19.5$ µm and $\bar{r} = r/R$ is the spatial position in the particle relative to the centre where $\bar{r} = 0$. Plotted are single transects across individual particles (black circles). The grey shaded area represents the standard error about the mean on repeat measurements. The interpolated mean of the data is the dashed curve. The red curve represents our model where Bi $\gg 1$ and the reaction rate is neglected (such that $C \to 0$ at $\bar{r} = 1$ and $\bar{r} = -1$ for all $\bar{t} > 0$), and the purple curve represents our model where Bi $= 4.02$.

This is the peer-reviewed, final accepted version for American Mineralogist, published by the Mineralogical Society of America.
The published version is subject to change. Cite as Authors (Year) Title. American Mineralogist, in press.
DOI: https://doi.org/10.2138/am-2021-7691. http://www.minsocam.org/

Table 2

T [K]
673
773
873
973
1073

T [K]
673
773
873
973
1073

$\overline{C_r}$

$\overline{C_r}$

This is the peer-reviewed, final accepted version for American Mineralogist, published by the Mineralogical Society of America.
The published version is subject to change. Cite as Authors (Year) Title. American Mineralogist, in press.
DOI: https://doi.org/10.2138/am-2021-7691. http://www.minsocam.org/

Results of analysis for temperature-dependent diffusivity

Monodisperse

$\langle R \rangle$ = 10.6 µm	$\langle R \rangle$ = 19.5 µm	$\langle R \rangle$ = 127.7 µm	
$\mathcal{D}$	$\mathcal{D}$	$\mathcal{D}$	Average
[$m^2.s^{-1}$]	[$m^2.s^{-1}$]	[$m^2.s^{-1}$]	[$m^2.s^{-1}$]
$2.25 \pm 0.25 \times 10^{-17}$	$3.49 \pm 0.75 \times 10^{-17}$	$1.43 \pm 0.65 \times 10^{-16}$	6.68×10^{-17}
$3.03 \pm 0.21 \times 10^{-16}$	$4.76 \pm 0.39 \times 10^{-16}$	$1.23 \pm 0.25 \times 10^{-15}$	6.70×10^{-16}
$7.12 \pm 1.23 \times 10^{-16}$	$3.35 \pm 0.36 \times 10^{-15}$	$6.86 \pm 1.11 \times 10^{-15}$	3.64×10^{-15}
$8.94 \pm 2.13 \times 10^{-15}$	$1.09 \pm 0.18 \times 10^{-14}$	$3.10 \pm 0.27 \times 10^{-14}$	1.70×10^{-14}
$2.64 \pm 0.94 \times 10^{-14}$	$2.64 \pm 0.39 \times 10^{-14}$	$1.06 \pm 0.12 \times 10^{-13}$	5.30×10^{-14}

Polydisperse

$\langle R \rangle$ = 10.6 µm	$\langle R \rangle$ = 19.5 µm	$\langle R \rangle$ = 127.7 µm	
$\mathcal{D}$	$\mathcal{D}$	$\mathcal{D}$	Average
[$m^2.s^{-1}$]	[$m^2.s^{-1}$]	[$m^2.s^{-1}$]	[$m^2.s^{-1}$]
$1.60 \pm 0.16 \times 10^{-18}$	$1.20 \pm 0.23 \times 10^{-18}$	$2.89 \pm 1.41 \times 10^{-18}$	1.90×10^{-18}
$2.96 \pm 0.58 \times 10^{-17}$	$1.65 \pm 0.13 \times 10^{-17}$	$4.49 \pm 0.84 \times 10^{-17}$	3.03×10^{-17}
$1.78 \pm 0.22 \times 10^{-16}$	$1.97 \pm 0.14 \times 10^{-16}$	$5.08 \pm 0.39 \times 10^{-16}$	2.94×10^{-16}
$3.67 \pm 1.19 \times 10^{-15}$	$2.21 \pm 0.62 \times 10^{-15}$	$5.57 \pm 1.16 \times 10^{-15}$	3.82×10^{-15}
$8.77 \pm 3.46 \times 10^{-15}$	$1.14 \pm 0.49 \times 10^{-14}$	$3.79 \pm 0.53 \times 10^{-14}$	1.94×10^{-14}

This is the peer-reviewed, final accepted version for American Mineralogist, published by the Mineralogical Society of America.
The published version is subject to change. Cite as Authors (Year) Title. American Mineralogist, in press.
DOI: https://doi.org/10.2138/am-2021-7691. http://www.minsocam.org/

Table 3

\beta
D_\beta
E

\beta
D_\beta
E

\gamma
D_\gamma
E

\gamma
D_\gamma
E

This is the peer-reviewed, final accepted version for American Mineralogist, published by the Mineralogical Society of America.
The published version is subject to change. Cite as Authors (Year) Title. American Mineralogist, in press.
DOI: https://doi.org/10.2138/am-2021-7691. http://www.minsocam.org/

Results of analysis for temperature- and concentration-dependent diffusivity

	Monodisperse			
	$\langle R \rangle$ = 10.6 µm	$\langle R \rangle$ = 19.5 µm	$\langle R \rangle$ = 127.7 µm	Average
[K]	14613.9 ± 1092.3	11324.2 ± 736.6	12075.5 ± 953.7	12671.2
[$m^2.s^{-1}$]	5.64 ± 3.83 x 10^{-8}	2.80 ± 1.46 x 10^{-9}	1.64 ± 0.98 x 10^{-8}	2.52 x 10^{-8}
[$kJ.mol^{-1}$]	121.51 ± 9.08	94.15 ± 6.12	158.70 ± 9.79	133.79

	Polydisperse			
	$\langle R \rangle$ = 10.6 µm	$\langle R \rangle$ = 19.5 µm	$\langle R \rangle$ = 127.7 µm	Average
[K]	17489.5 ± 1498.1	18625.5 ± 1855.3	19087.2 ± 1178.3	18400.7
[$m^2.s^{-1}$]	3.64 ± 2.88 x 10^{-7}	1.03 ± 0.87 x 10^{-6}	4.33 ± 2.91 x 10^{-6}	1.91 x 10^{-6}
[$kJ.mol^{-1}$]	145.42 ± 12.46	154.86 ± 15.43	158.70 ± 9.80	152.99

	Monodisperse			
	$\langle R \rangle$ = 10.6 µm	$\langle R \rangle$ = 19.5 µm	$\langle R \rangle$ = 127.7 µm	Average
[K]	15180.2 ± 1353.4	10222.2 ± 1019.2	12415.3 ± 917.4	12605.9
[$m^2.s^{-1}$]	6.70 ± 5.04 x 10^{-8}	.57 ± 4.23 x 10^{-10}	1.76 ± 1.03 x 10^{-8}	2.84 x 10^{-8}
[$kJ.mol^{-1}$]	126.22 ± 11.25	84.99 ± 8.47	103.23 ± 7.63	104.81

	Polydisperse			
	$\langle R \rangle$ = 10.6 µm	$\langle R \rangle$ = 19.5 µm	$\langle R \rangle$ = 127.7 µm	Average
[K]	17046.9 ± 1444.1	17421.0 ± 1603.5	19590.7 ± 1238.9	18139.5
[$m^2.s^{-1}$]	1.48 ± 1.15 x 10^{-7}	2.26 ± 1.82 x 10^{-7}	5.16 ± 3.57 x 10^{-6}	1.84 x 10^{-6}
[$kJ.mol^{-1}$]	141.74 ± 12.01	144.85 ± 13.33	162.89 ± 10.30	149.83

This is the peer-reviewed, final accepted version for American Mineralogist, published by the Mineralogical Society of America.
The published version is subject to change. Cite as Authors (Year) Title. American Mineralogist, in press.
DOI: https://doi.org/10.2138/am-2021-7691. http://www.minsocam.org/

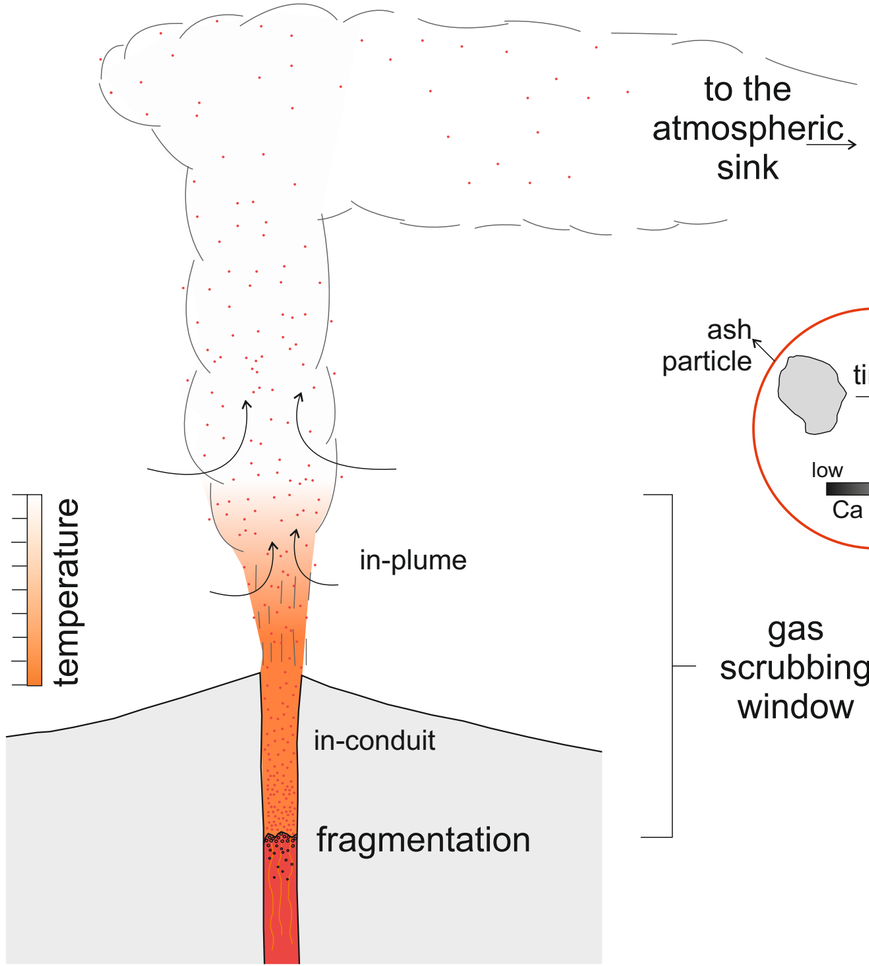

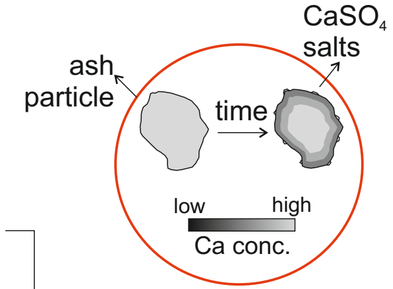

gas scrubbing window

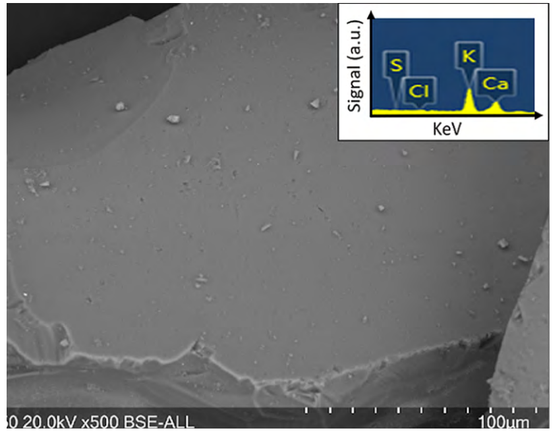

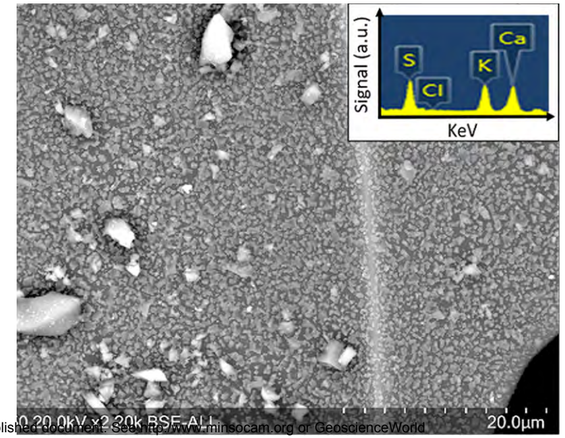

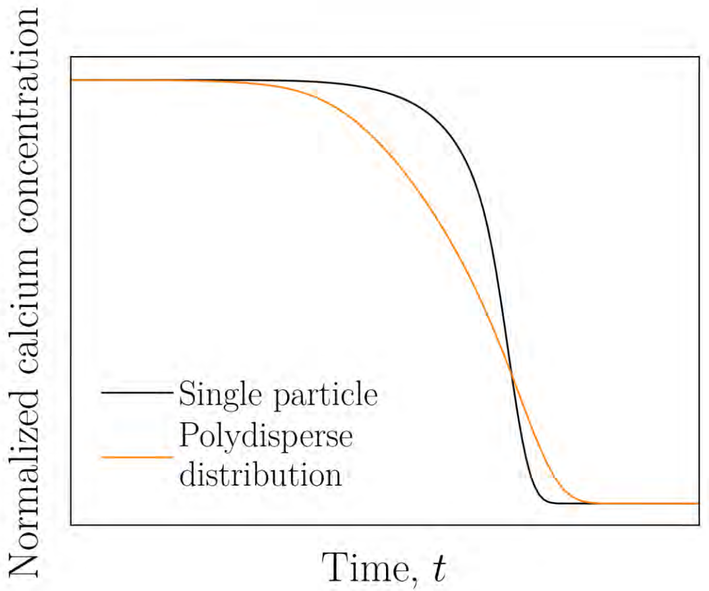

This is the peer-reviewed, final accepted version for American Mineralogist, published by the Mineralogical Society of America.
The published version is subject to change. Cite as Authors (Year) Title. American Mineralogist, in press.
DOI: https://doi.org/10.2138/am-2021-7691. http://www.minsocam.org/

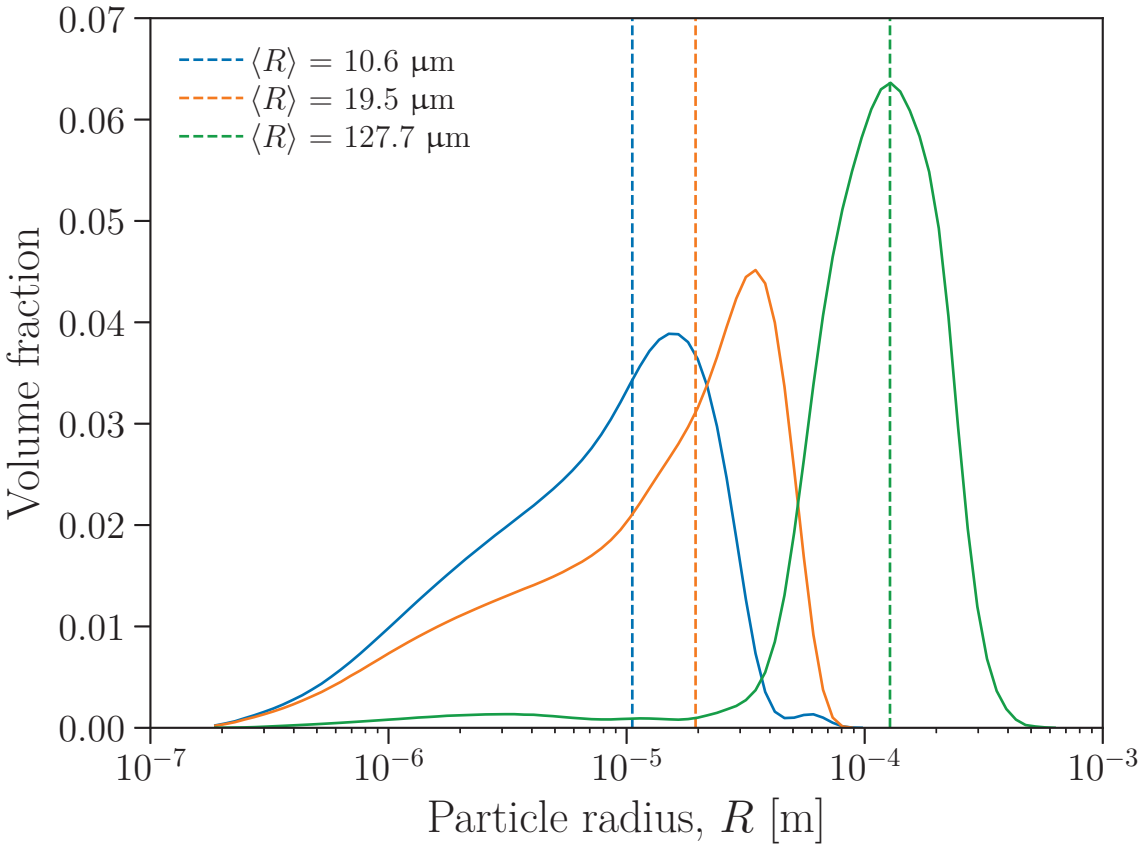

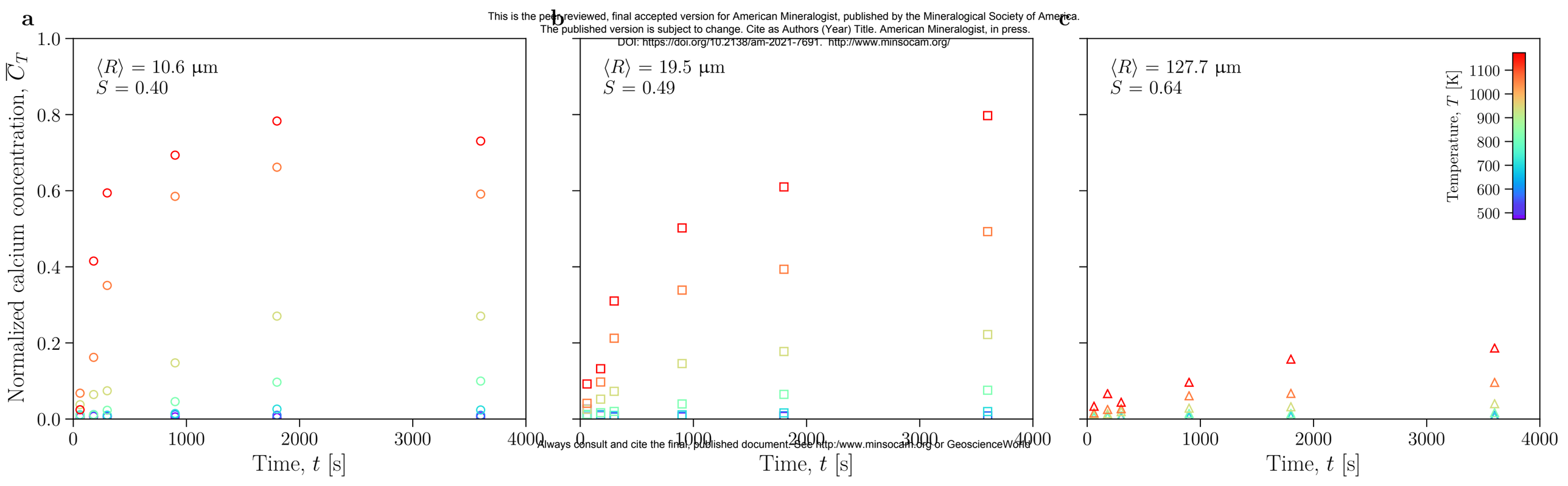

This is the peer-reviewed, final accepted version for American Mineralogist, published by the Mineralogical Society of America.
The published version is subject to change. Cite as Authors (Year) Title. American Mineralogist, in press.
DOI: https://doi.org/10.2138/am-2021-7691. http://www.minsocam.org/

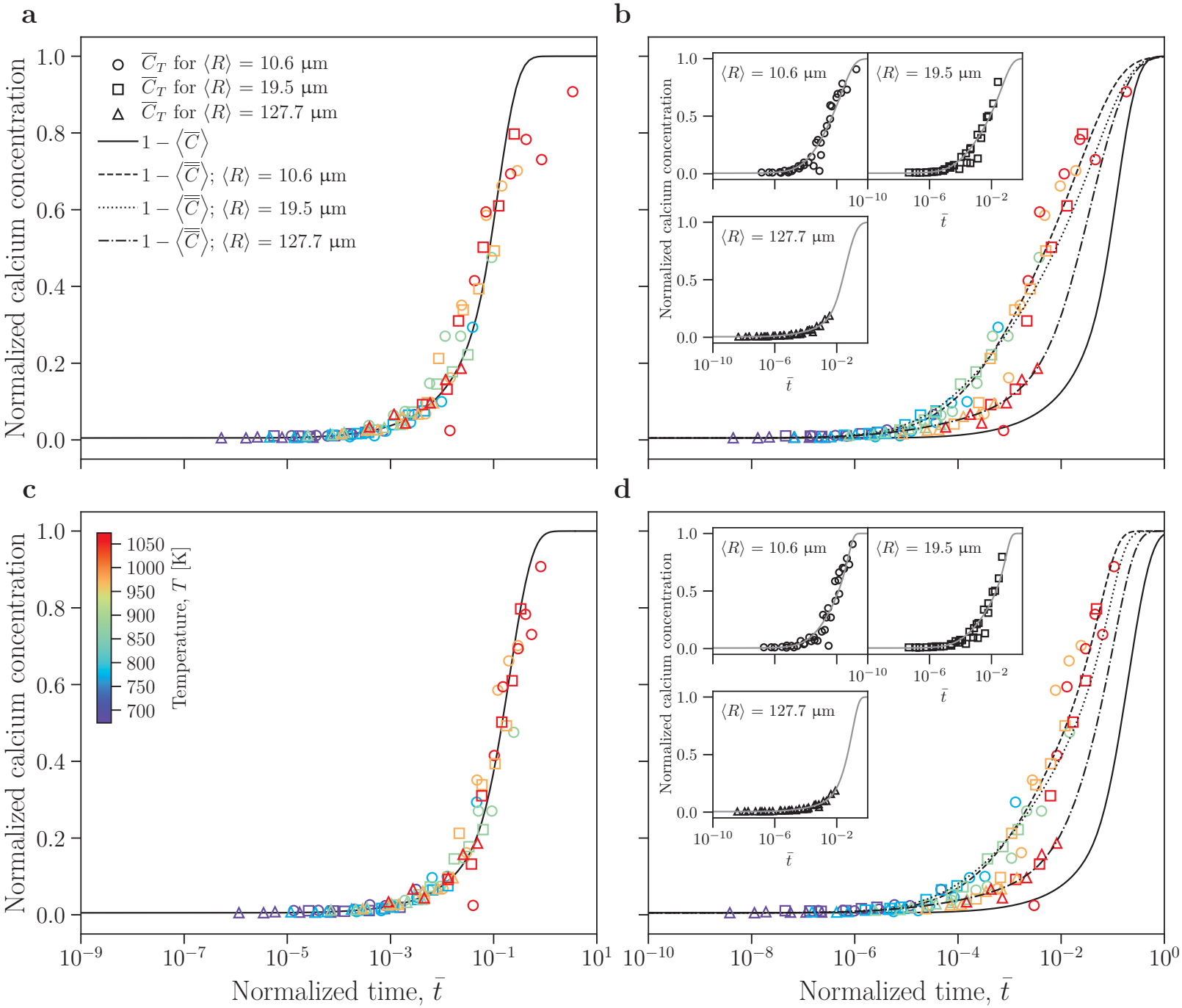

This is the peer-reviewed, final accepted version for American Mineralogist, published by the Mineralogical Society of America.
The published version is subject to change. Cite as Authors (Year) Title. American Mineralogist, in press.
DOI: https://doi.org/10.2138/am-2021-7691. http://www.minsocam.org/

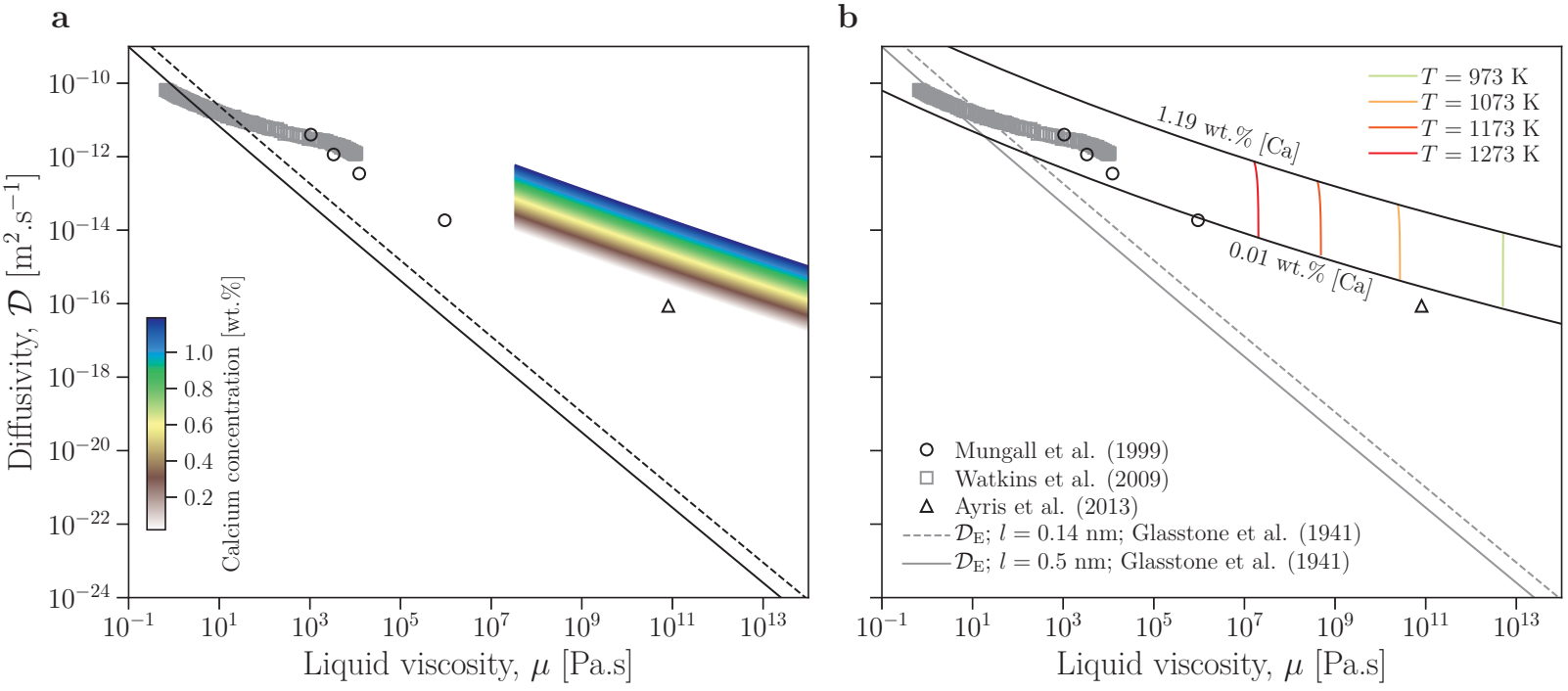

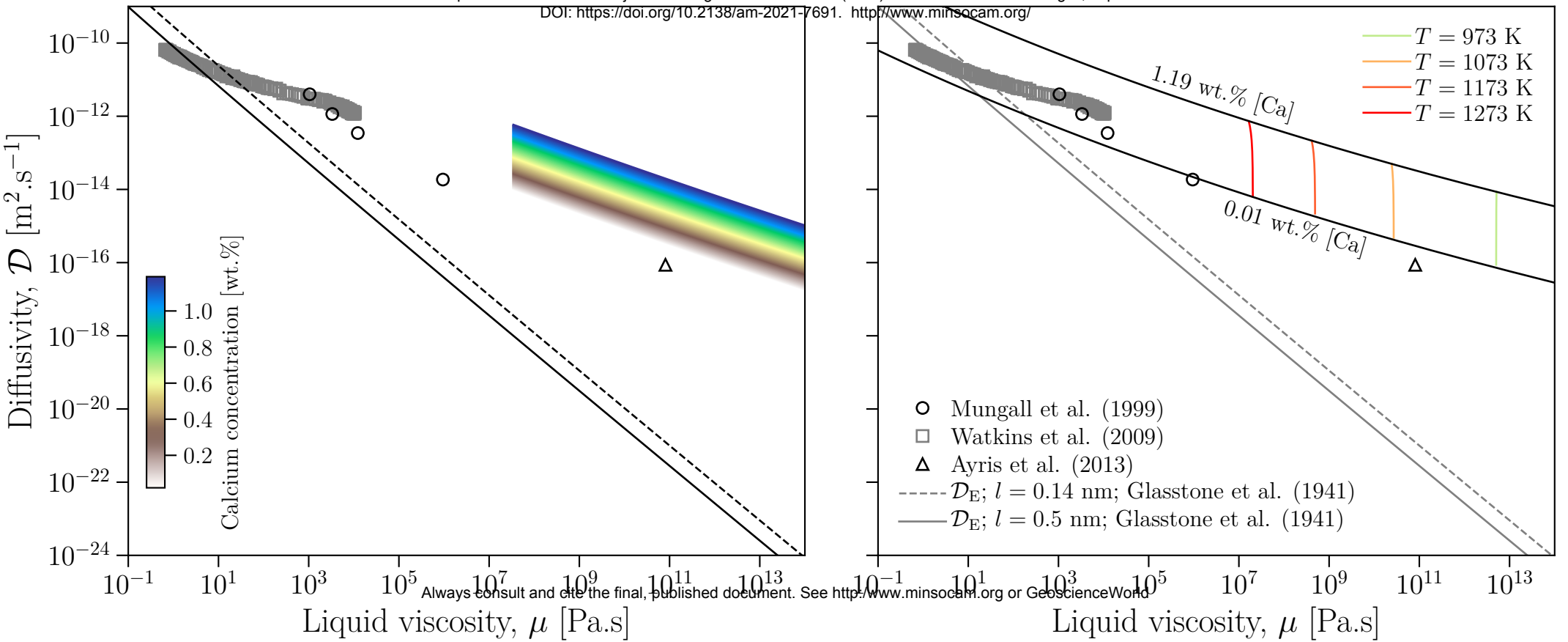

This is the peer-reviewed, final accepted version for American Mineralogist, published by the Mineralogical Society of America.
The published version is subject to change. Cite as Authors (Year) Title. American Mineralogist, in press.
DOI: https://doi.org/10.2138/am-2021-7691. http://www.minsocam.org/

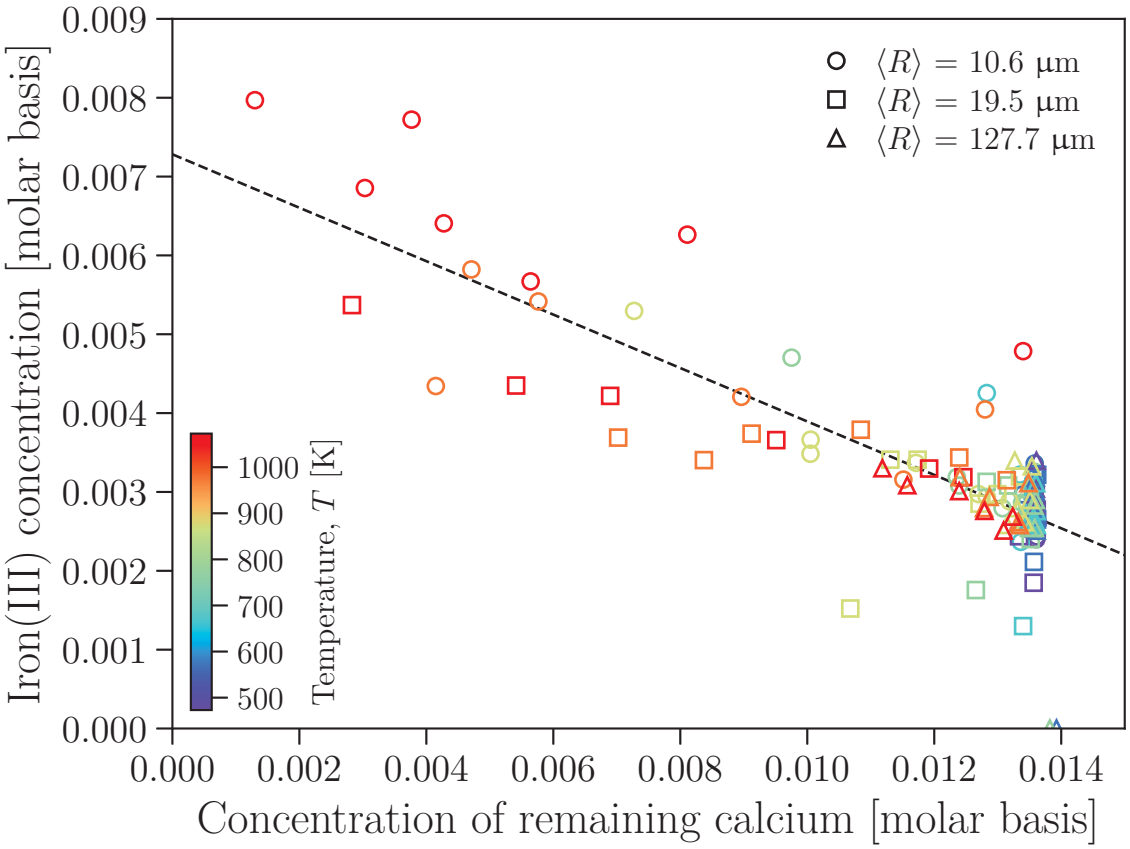

This is the peer-reviewed, final accepted version for American Mineralogist, published by the Mineralogical Society of America.
The published version is subject to change. Cite as Authors (Year) Title. American Mineralogist, in press.
DOI: https://doi.org/10.2138/am-2021-7691. http://www.minsocam.org/